Compositional controls on the thermal conductivity of metamorphic rocks

Thesis submitted in accordance with the requirements of the University of Adelaide for an Honours Degree in Geophysics

Celina Adele Rosa Sanso

November 2019

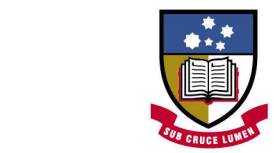

THE UNIVERSITY *of* ADELAIDE

COMPOSITIONAL CONTROLS ON THE THERMAL CONDUCTIVITY OF METAMORPHIC ROCKS

THERMAL CONDUCTIVITY OF METAMORPHIC ROCKS

ABSTRACT

Thermal conductivity is essential for determining heat flow within the Earth, which is necessary for geothermal investigations, accurately modelling tectonic and volcanic processes, and predicting petroleum maturation. Although currently, conductivity can be measured on hand samples, it can be impracticable to make regional and subsurface models due to time and expense required. In this study, an analysis on the compositional controls on thermal conductivity of metamorphic rocks is completed. Thermal conductivity was determined using an optical thermal scanner on 168 metamorphic samples with prior major oxide element analyses. Density is determined through models, as well as measured using Archimedes' principle. The results show that thermal conductivity varies between 1.698 to 5.226 W m^{-1} K^{-1}. When observing the relationships there is no trend between thermal conductivity and the major oxides. However, anisotropy has a log normal distribution with a mean of -2.098 and a standard deviation of 1.346, and produces a weak negative correlation with conductivity of -0.566. A correlation occurs between SiO_2 and K_2O, where a maximum anisotropy potential peaks between 60% to 65%, and approximately 5%, respectively. The modelled density is successful in determining the measured density, allowing the density for future samples to be determined indirectly. From the results of the study, more considerations need to be taken when observing the compositional controls in the future for metamorphic rocks. A narrower range of rock types or chemistry could be considered, along with the mineralogy of the samples. Singular provinces should also be considered to determine if conductivity for metamorphic rocks occur regionally. Furthermore, a focused study on how the P-T conditions of a singular rock type change with thermal conductivity can be assessed. Such analyses will improve estimates of subsurface conductivity and the ability to accurately estimate crustal temperatures.

KEYWORDS

Thermal conductivity, anisotropy, metamorphism, composition, mineralogy, density

Table of Contents

List of Figures

List of Tables

INTRODUCTION

Thermal conductivity (k) is a measure of how easily heat is transmitted through a material, and is essential for: determining rates of heat loss from the surface of the Earth, geotherms, modelling tectonic and volcanic processes, and predicting oil maturation (Schön, 2015b). Previous studies of metamorphic rocks suggest quartz fraction controls the thermal conductivity within the sample (Clauser, 2009, 2011; Clauser & Huenges, 1995; Kukkonen, Jokinen, & Seipold, 1999; Pribnow & Umsonst, 1993). However, not all metamorphic samples contain quartz and therefore quartz does not control the conductivity in this case. A similar study by Jennings, Hasterok, & Payne, (2019) analysed plutonic rocks and it was determined that the SiO_2 influences the conductivity because of the large abundance of SiO_2 over the entire compositional range.

The thermal conductivity of metamorphic rocks also vary parallel and perpendicular to the foliation (Clauser, 2009, 2011; Clauser & Huenges, 1995; Davis, Chapman, Van Wagoner, & Armstrong, 2007; Horai, 1971; Schön, 2015b). This behaviour is known as anisotropy (α). Anisotropy is defined as a directional dependence of tensorial properties, with the opposite of anisotropy being isotropy (Schön, 2015a). An isotropic material is when at any point, a vectorial property has the same magnitude in all directions. If there is a difference in magnitude and the directional dependence between the vectors, then the material is anisotropic. To calculate the anisotropy for thermal conductivity, the following ratio is used,

$$\alpha = \frac{k_{\parallel}}{k_{\perp}} \tag{1}$$

where $k_{\parallel}$ is the parallel conductivity and $k_{\perp}$ is the perpendicular conductivity. In general, $k_{\parallel}$ is larger than $k_{\perp}$. The values of anisotropy for metamorphic rocks is $>$ 0, where 1 is completely isotropic and any value ≤ 0.9 or ≥ 1.1 is anisotropic (Davis

et al., 2007; Vosteen & Schellschmidt, 2003). In addition to this, anisotropy for metamorphic rocks can exist on multiple scales from microscopic scale, laboratory scale (> cm's), or tectonic scale (> km's) (Clauser & Huenges, 1995). For this study, anisotropy will only be considered on a laboratory scale.

Anisotropy can also be affected by the foliation of the sample and the degree of orientation of the grains (Abdulagatova, Abdulagatov, & Emirov, 2009; Davis et al., 2007; Vosteen & Schellschmidt, 2003). Foliation refers to a change of composition or material, and lineation refers to how the minerals in the samples are aligned. Both of these factors are determined by what minerals are present when the rock forms. Furthermore, the foliation effects the conductivity of rocks as centimetre thick bands of a single mineral can change the conductivity greatly because minerals are compositionally diverse compared to bulk rock averages (Balkan, Erkan, & Şalk, 2017; Clauser, 2011). Orientated grains direct heat flow efficiently through rocks, whereas randomly orientated grains do not, thus effecting the degree of conductivity (Abdulagatova et al., 2009).

It is not possible to make direct measurements of the present lower crust due to the challenges of sampling below 5 km. Therefore, thermal conductivity must be indirectly calculated with mixing models, along with knowledge of the mineralogy, composition, porosity, density, and P-wave velocity (Chopra et al., 2018; Clauser, 2011; Clauser & Huenges, 1995; Jennings et al., 2019; Ray et al., 2015; Schön, 2015b). The mixing models are based on averaging conductivity of components in various ways (Abdulagatova et al., 2009). The various ways indicate the multiple types of models which can be used, for example, the harmonic mean, arithmetic mean, and geometric mean.

The aims of this study are to develop a empirical model for predicting thermal conductivity of metamorphic rocks as a function of composition. In addition to this, compositions that are most susceptible to anisotropy will be identified and it will be determined if there is a quantitative relationship between composition and the

magnitude of anisotropy. In this study, samples of metamorphic rocks originating from Australia, Antarctica, Italy, Argentina, and India have been analysed. The selection of samples contain 151 metasediments and 17 metaigneous rocks with the metamorphic grade ranging from greenschist to amphibolite and granulite facies.

BACKGROUND

There are a number methods which can be used to measure thermal conductivity (Birch, 1950; Horai, 1971; Popov, 1983). The methods fall within two main techniques: steady-state (the divided-bar method and the needle probe method), and transient (line-source methods, ring-source methods and the optical scanning method) (Clauser, 2009, 2011; Fuchs, Schütz, Förster, & Förster, 2013; Popov, Pribnow, Sass, Williams, & Burkhardt, 1999; Pribnow & Umsonst, 1993; Ray et al., 2015). The steady-state technique indicates there is no change in the rock at any point in time, meaning the heat applied to the rock is constant (Chopra, Ray, Satyanarayanan, & Elangovan, 2018). The transient technique implies there is a variation in thermal state over time, indicating the change in temperature determines the conductivity (Chopra et al., 2018). However, only the divided-bar, needle probe and optical scanning methods are recommended by the International Society for Rock Mechanics (ISRM) to measure thermal conductivity at atmospheric pressure conditions in a laboratory (Popov Beardsmore, Clauser, & Roy, 2016).

To show the difference between the steady-state and transient methods, the divided-bar method and optical scanning method are compared in this study. The method for the divided-bar involves drill core samples that are cut into small cylinders and placed between two standards of known conductivity as shown in Figure 1A (Beck & Beck, 1965; Birch, 1950; Clauser, 2009; Horai & Baldridge, 1972a, 1972b; Kukkonen et al., 1999; Popov et al., 1999; Schön, 2015b). One of the reference cylinders is then heated and once it reaches steady state, the temperature drop in the sample is

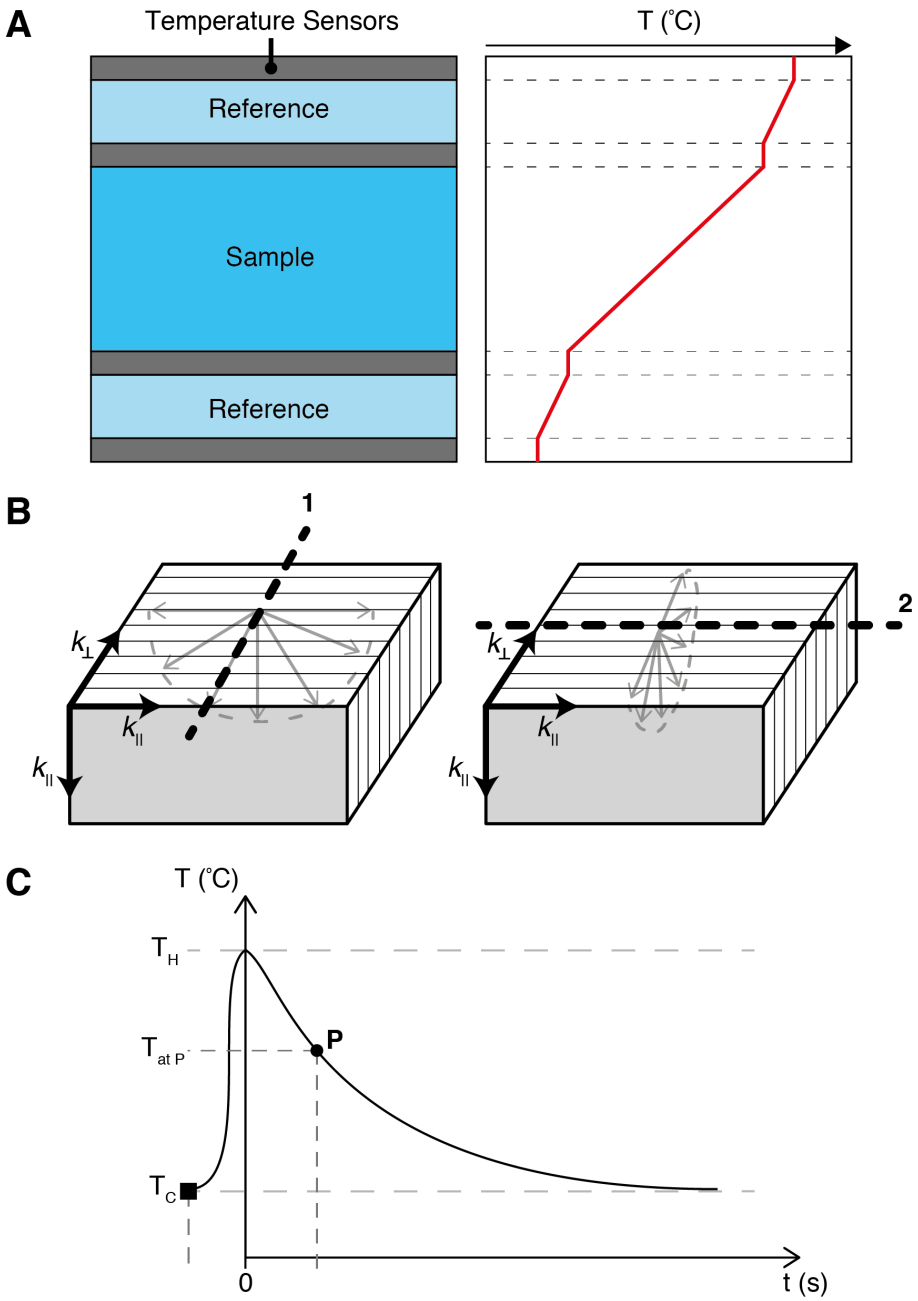

Figure 1: The divided-bar (**A**) and optical scanning method (**B**, **C**). **A**: A heat source is continuously applied at one end until the heat is transferred to the other side (modified from Schön, 2015b). Thermal conductivity is determined by the temperature gradient of the sample. **B**: Scan line 1 (k_{app1}) and scan line 2 (k_{app2}) for the case of 2D anisotropy. Thin black lines represent the foliation. Radial arrows show the plane of heat flow through the sample during scanning (modified from Popov et al., 2016). **C**: The temperature curve measured for point P. The square indicates the passing of the cold temperature sensor and the circle is the passing of the hot temperature sensor.

then measured, as shown by the temperature gradient for the sample in Figure 1A. The temperature drop in the standards and the samples are then compared to give the conductivity of the sample.

The optical scanning method is shown in Figure 1B and 1C (Clauser, 2009; Fuchs et al., 2013; Popov, 1983; Popov et al., 1999; Popov et al., 2016; Schön, 2015b). Samples are placed on a stage, where the mobile source contains infra-red temperature sensors and heat source move beneath the samples and record the change in temperature. In the case of foliated metamorphic rocks, a minimum of two dimensions need to be considered due to the anisotropy. The scan line perpendicular to the foliation (Figure 1B, scan line 1) provides k_{app1} and the parallel scan line (Figure 1B, scan line 2) produces k_{app2}. The temperature recorded is at point P in Figure 1C, which is then applied to a simple heat flow equation to determine the conductivity of the sample (Popov, 1983).

From various sources, results have shown that thermal conductivity depends on numerous parameters such as: chemical and mineral composition, fluid content, porosity, pressure, temperature, isotropy, homogeneity, density, structure, fractures, and degree of crystallisation (Balkan et al., 2017; Clauser, 2011; Clauser & Huenges, 1995; Khandelwal, 2011). However, each parameter contributes differently when measuring conductivity with the four main rock groups: sedimentary, volcanic, plutonic, and metamorphic (Clauser, 2009, 2011). Sedimentary rocks are controlled by porosity, sediment type, and dominant mineral phases, and porosity governs volcanic rocks. Plutonic rock conductivity is primarily controlled by the percentage of feldspar and in metamorphic rocks, conductivity depends on the amount of quartz in the sample (Clauser, 2009, 2011).

Vosteen and Schellschmidt (2003) determined the influence of thermal conductivity on samples measured at various temperature intervals on 118 samples. They found the temperature dependence is different for crystalline rocks and sedimentary rocks between 0°C and 500°C. However, both rock types show a general trend of decreasing

conductivity with increasing temperature of the sample. The conductivity values for both crystalline and sedimentary samples range between 2 to 6 W m^{-1} K^{-1} using the needle probe method. They also found anisotropy factors lower than 0.9 and greater than 1.1 has a significant effect on the conductivity (with 1 representing an isotropic sample).

To determine thermal conductivity indirectly, the most frequently used method is mixing models, (Abdulagatova et al., 2009; Chopra et al. 2018; Clauser 2009, 2011; Clauser & Huenges, 1995; Fuchs et al., 2013; Jennings et al., 2019; Pribnow & Umsonst, 1993; Ray et al., 2015; Schön, 2015b). Pribnow and Umsonst (1993) used the four most common mixing models: geometric mean, arithmetic mean, harmonic mean and the Hashin and Shtrikman mean. The results showed the geometric mean gives the best result. In addition to this, Ray et al. (2015) also used these four mixing models along with the effective-medium theory mean for 26 rock samples of granulite facies from the Southern Granulite Province, India. The conductivities ranged between 2.4 and 3.5 W m^{-1} K^{-1}. The study incorporated the mineralogy of the samples and mineral thermal conductivity with the mixing models, where the harmonic mean was the most precise mixing model. These two studies have contradicting mixing model results, indicating more analyses need to be undertaken to determine conductivity indirectly.

Jennings et al. (2019) showed how the oxide composition of rocks is related to thermal conductivity. They studied 340 igneous samples using an optical scanner, with 122 additional data from various literature. The aim of the study was to produce a empirical relationship between composition and conductivity using major oxide composition, CIPW normative mineralogy and estimated modal mineralogy. The four mixing models applied were the arithmetic mean, harmonic mean, geometric mean, and square-root mean because each model can be easily linearised. The results showed the geometric model produces the best fit, with the primary control on the samples being SiO_2. In addition to the composition and mineralogy, P-wave

velocity and density was also modelled with thermal conductivity. The empirical model showed when the P-wave velocity is within range of 6 to 8 km s^{-1}, conductivity can be calculated to within 0.31 W m^{-1} K^{-1}. For four compositional groups (low-Mg silicates, high-Mg silicates, igneous carbonates and sedimentary carbonates), a density model was developed using multiple linear regression for each group (Hasterok, Gard, & Webb, 2018; Jennings et al., 2019). The results show with increasing density, thermal conductivity decreases until 3000 kg m^{-3}, and above 3000 kg m^{-3}, conductivity then increases. With the success of Jennings et al. (2019) empirical model with igneous rocks, it is reasonable to assume a similar study with metamorphic rocks should produce similar results, which forms the basis of the present study.

Sample selection and characteristics

Due to the numerous properties which can influence thermal conductivity, a number of the parameters indicated above will be constrained for the samples used in this study. The primary focus of this study will be on metasedimentary rocks, with an additional 17 metaigneous rocks, where all samples are crystalline and have no visible fractures (see Appendix C for sample details). In addition to this, unsaturated conductivity measurements will be undertaken on the samples as porosity is typically $<<$ 4% visually and is below the threshold for accurate saturated measurements. Therefore, porosity and fluid content will not be considered within the study. All samples were measured at room temperature and pressure. For the study, conductivity, density and estimated mineralogy were conducted on every sample. The optical scanning method was chosen due to its short measuring time, no contact between the sensors and the sample, and the ability to measure the anisotropic components of the samples (Popov et al., 2016). In addition to this, an optical scanner can determine conductivity within a 3% uncertainty (Popov et al., 2016). The compositional range is shown in Figure 2 using the major oxide geochemistry

(see Appendix E for major oxide data) of the metasedimentary samples, where most are SiO_2 rich.

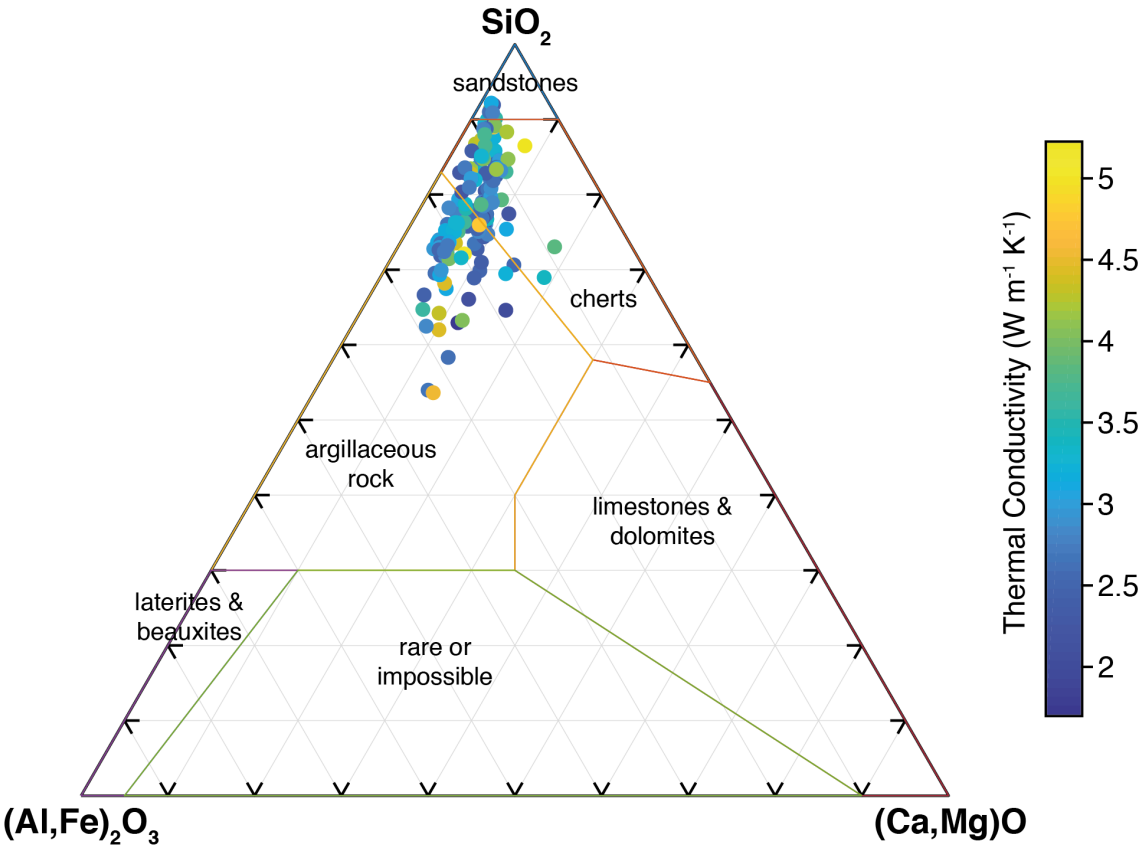

Figure 2: A ternary diagram showing the compositional range of samples used in this study (modified from Mason, 1952; Turekian 1969). Plotted relative to sedimentary rock composition fields. The thermal conductivity values for each sample are the values from the bulk thermal conductivity model described in the method.

To assist with the mixing models, principal components analysis (PCA) can be used to establish which compositional components have a large impact on the thermal conductivity values. PCA is a standard statistical tool used for multivariate data analysis (Shlens, 2014; Wold, Esbensen, & Geladi, 1987). The goal of implementing PCA is to find relationships between objects by: simplification of the data, data reduction, modelling, outlier detection, variable selection, classification, prediction, or unmixing on the data. When PCA analysis is undertaken, the data is first broken down into the proportion of variance within each principal component (PC), and

then the highest variance percentage in each component is compared against the others (Ringnér, 2008). With each vector formed by the components, two variables can be analysed, allowing the data to reduce by one dimension. The largest variation in the reduced data is shown by the magnitude of the vectors (Ringnér, 2008). Henceforth, the set of vectors formed should describe the chemical variations from most to least important in this study. If the composition does effect thermal conductivity for the selected samples, then it is expected that one of the components should correlate with conductivity.

METHODS

Thermal conductivity measurements

SAMPLE PREPARATION

Due to the anisotropy within metamorphic rocks, the samples were first cut by a rock saw with a diamond drill perpendicular to the plane of foliation. The size of the samples were in accordance with the parameters provided by Popov et al. (2016) in Table 1. Samples smaller than the sizes provided under *Acceptable dimensions of rock samples studied* in Table 1, do not give accurate readings of thermal conductivity because the heat will diffuse out of the sample.

STATISTICAL ANALYSIS ON METHODS

Two methods are proposed for measuring the samples on the Thermal Conductivity Scanner (TCS) (owned by the South Australian Centre for Geothermal Research): 1) three lines parallel and perpendicular to the foliation were measured three times (referred to as method 1); 2) nine lines parallel and perpendicular to the foliation

Table 1: Specifications and sensitivity of a type 3 optical thermal scanner used in this study (Popov et al., 2016).

Parameter	Type 3
Accuracy; precision	
Thermal conductivity [W m^{-1} K^{-1}]	±1.5; ±1
Thermal diffusivity (mm^2s^{-1})	±2.5; ±2
Volumetric heat capacity [$MJ(m^{-3}K^{-1})$]	±3; ±2.5
Measured thermal property ranges	
Thermal conductivity [W m^{-1} K^{-1}]	0.2 - 45
Thermal diffusivity (mm^2s^{-1})	0.092 - 5.0
Volumetric heat capacity [$MJ(m^{-3}K^{-1})$]	0.8 - 4.0
Maximum total length of scanning line (mm)	900
Maximum number of samples for simultaneous measurements	30
Total time of measurement of 1 full set of rock samples on platform (s)	230
Acceptable dimensions of rock samples studied	
Length (min-max) (mm)	8 - 900
Width (min-max) (mm)	8 - 200
Thickness (min-max) (mm)	6 - no limit
Ranges of thermal properties of reference standards	
Thermal conductivity [W m^{-1} K^{-1}]	0.195 - 45
Thermal diffusivity (mm^2s^{-1})	0.092 - 5.0
Form of the rock sample surface under measurement	Flat, cylindrical
Possibility to perform thermal property measurements on dry and fluid-saturated rock samples	Yes

were measured (referred to as method 2). Statistical analyses for the mean and standard deviation were performed on each method using MATLAB R2018b. Method 1 has an average mean of 2.999 and an average standard of 0.526. For method 2, the average mean and standard deviation is 3.002 and 0.29, respectively. The analysis in Figure 3 shows there is a more restricted range of average thermal conductivity in method 1 than in method 2. However, method 2 has a smaller average

standard deviation. Method 2 was the selected scanning method for this study, as its large variation in conductivity reflects the physical and chemical properties of metamorphic rocks more precisely.

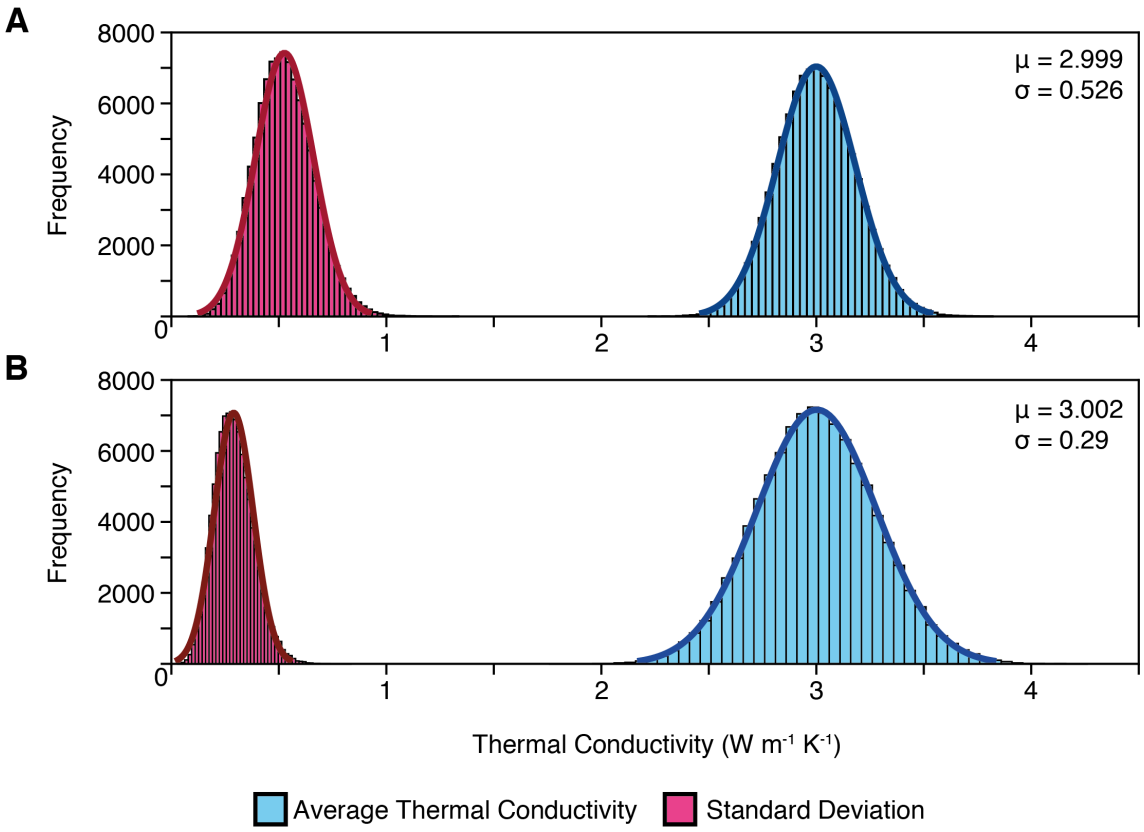

Figure 3: The statistical analysis on the two proposed methods: method 1 and method 2. **A**: method 1 shows a restricted range of average thermal conductivity, but has a higher standard deviation average. **B**: method 2 has a smaller standard deviation average, however, there is a larger deviation of the average thermal conductivity. Method 2 is the selected method for this study due to the smaller deviation, and metamorphic rocks are heterogeneous which produces a larger range of thermal conductivity values.

MEASURING THERMAL CONDUCTIVITY

The method for measuring thermal conductivity is described by Popov et al. (2016), however modifications have been made. Before the samples are placed on the stage, the scanning surface of the sample is brushed down to remove any contamination.

The surface is then covered completely with 3M 50 Series Matte Black vinyl film to ensure the heat from the thermal source spreads evenly. Usually, black paint is applied to the scanning surface, but it has been proven that this film is just as accurate (Jennings et al., 2019). Furthermore, the film requires less preparation and no cleaning once the scan has been completed.

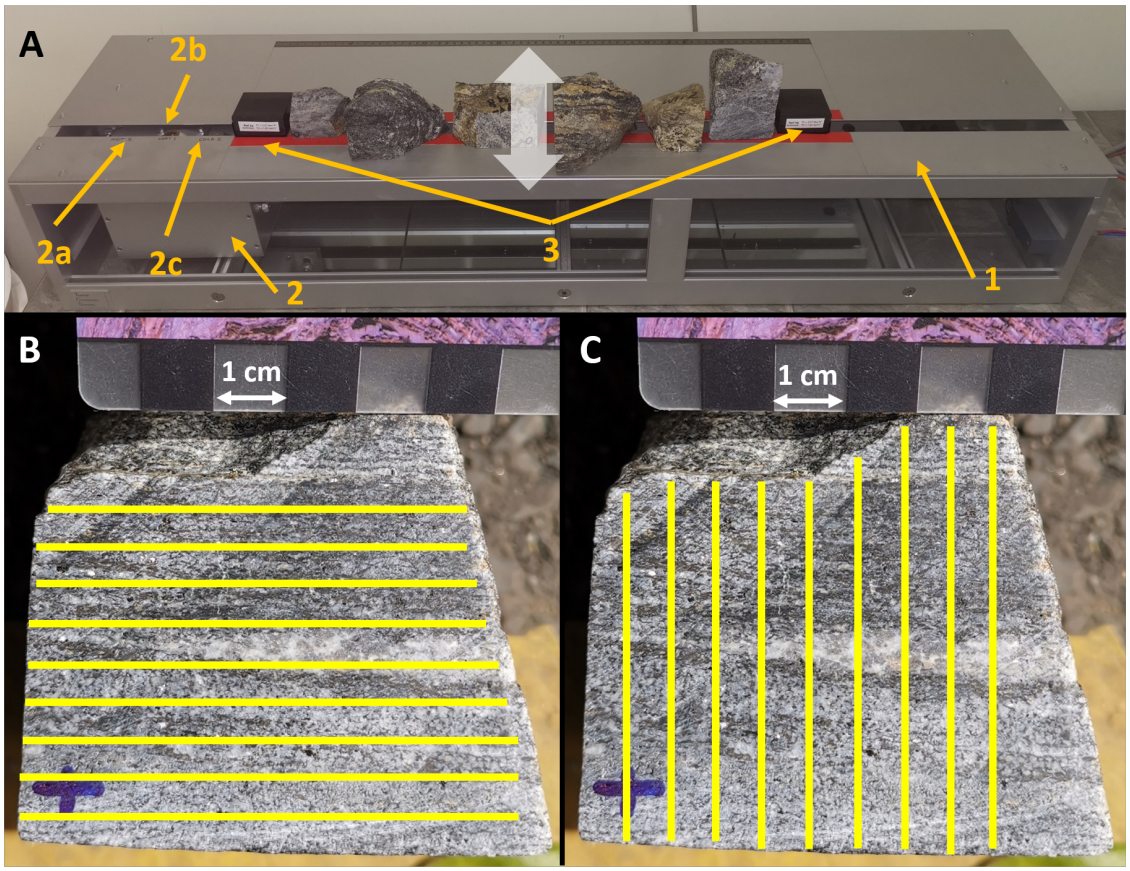

Figure 4: **A**: The optical scanner: (1) the stage; (2) mobile source; (2a) hot temperature sensor; (2b) the heat source; (2c) cold temperature sensor; (3) reference standards. Sample scanning surface are first covered with 3M 50 Series Matte Black Vinyl film before being placed on the optical scanner. The white arrow indicates the direction of movement for changing the scan line. Samples shown in figure (left to right): WI-01, WI-07, WI-48, WI-99, WI-62, LM-08. **B**: The scanning lines on sample LM-08, using method 2. 9 scanning lines parallel to the foliation, where scan lines are to size. **C**: 9 scanning lines perpendicular to the foliation, using method 2, with scan lines to size.

Samples were placed scan face down on the stage along with the TCS reference standards at each end of the scanner (Figure 4A). To get the best result, the standards

must have similar conductivity to the samples. The TCS standards used for this study are Ref. 3a and Ref. 3b with the standard at 2.37 W m^{-1} K^{-1}. For samples which have a conductivity greater than 4.1 W m^{-1} K^{-1}, standards Ref. 4a and Ref. 4b were used with the standard measured at 5.94 W m^{-1} K^{-1}. The samples were first measured parallel to the foliation (Figure 4B), and then repeated perpendicular to the foliation (Figure 4C). For each scan line, the samples are moved equally nine times as shown in Figure 4A.

The conductivity measurements recorded are: k_{app1}, perpendicular to foliation reading (line 1 in Figure 1B), and k_{app2}, parallel to foliation reading (line 2 in Figure 1B). To determine the parallel ($k_{\parallel}$) and the perpendicular conductivity ($k_{\perp}$), the following equations are used (Popov et al., 2016):

$$k_{\parallel} = k_{app1} \tag{2}$$

$$k_{\perp} = \frac{{k_{app2}}^2}{k_{app1}} \tag{3}$$

From the individual $k_{\parallel}$ and $k_{\perp}$ values, the anisotropy is calculated for each sample using Equation 1. To be able to analyse the anisotropy clearly, the absolute values of α were taken using the equation:

$$A = \frac{\max(k_{\parallel}, k_{\perp})}{\min(k_{\parallel}, k_{\perp})} \tag{4}$$

where A is the absolute anisotropy. For these values, 0 represents isotropy and any values ≥ 0.1 indicates an effect of anisotropy within the sample.

Bulk thermal conductivity model

To make the processing of thermal conductivity data simpler, and to allow for plots of combined $k_{\parallel}$ and $k_{\perp}$ values, the geometric mean is used. This mean was chosen because the harmonic mean will give $k_{\perp}$ and the arithmetic mean produces $k_{\parallel}$. Therefore, to find a bulk average, the geometric mean calculation is applied for each sample:

$$k_{geo} = (k_{\perp} k_{\parallel}^2)^{\frac{1}{3}} \tag{5}$$

Density

Archimedes' principle was used to determine the density by measuring the dry and submerged weight of the samples when wet. A three-beam balance was used to weigh each sample. The equation used to calculate the density is:

$$\frac{\rho_{rock}}{\rho_{water}} = \frac{m_{dry}}{m_{dry} - m_{wet}} \tag{6}$$

where ρ is density (kg m^{-3}) and m is mass (g).

Modal mineralogy

The mineral assemblages for most samples were known from previous studies (see Appendix C for references and Appendix F for mineralogy), however the mineral modal proportions are mostly unknown. The modal mineralogy was determined by two different methods: HyLogger analysis and by pixel counting images of the samples. For more details on each of these methods, see Appendix A.

HYLOGGER

The HyLogger is regarded as the industry standard for efficient mineral proportion detection (CSIRO, 2018). The instrument is located at the South Australian Drill Core Library. The HyLogger is a hyperspectral logger that uses visible and infrared light to characterise minerals from hand samples, rock chips and drill core (CSIRO, 2018). The spectra collected from the HyLogger is processed via The Spectral Geologist 8 (TSG 8), a software tool, and compared with a database of mineral spectra. Unfortunately, when analysing the samples for this study, the HyLogger analysis did not detect minerals that were clearly evident in the samples, and identified minerals that did not exist in the samples. From these analyses, the HyLogger is not a useful tool to determine mineral proportions.

PIXEL COUNTING

The lack of success from the HyLogger lead to the pixel counting method to determine the modal mineralogy of the samples. Pixel counting uses an image of the sample and the modal mineralogy is calculated by the colour of the pixels relating to a mineral. To implement pixel counting, Adobe Photoshop was used in this study to analyse images of samples with known mineralogy. Once all pixels of a mineral were selected, statistical analysis was applied to determine the modal mineralogy. This method is ideal when the mineral assemblage is known, however due to time constraints in processing, only 13 out of 168 samples could be characterised by pixel counting.

RESULTS

Thermal conductivity

To understand relationships between the parameters analysed in this study, the geometric mean was used as an average between $k_{\parallel}$ and $k_{\perp}$, and will be referred to as k_{geo} (Equation 5). The largest k_{geo} value is 5.22 W m^{-1} K^{-1} for sample ST16-1 and the sample with the smallest conductivity is A222-018 at 1.69 W m^{-1} K^{-1}. The k_{geo} results were first compared with the major oxide composition within a metasedimentary ternary diagram, as shown in Figure 2. Metasedimentary samples in the study contain $\geq$ 50% SiO_2, and generally contain more $(Al,Fe)_2O_3$ than (Ca,Mg)O. For the conductivity values of each sample, there is no clear correlation between the two parameters. This result is further supported by Figure 5, which indicates no trend with both metasedimentary and metaigneous samples between the major oxides. The table of thermal conductivity results is shown in Appendix B.

Anisotropy

The anisotropic ratio values of all samples can be found in Appendix B, and all anisotropy values referred to from this point will be the absolute anisotropy (Equation 4). Sample 3-6 has the largest anisotropy at 2.730 and the smallest ratio is 9×10^{-4} for sample A325/121. As mentioned in the method, anisotropy values ≥ 0.1 are anisotropic, hence in this study, 97 samples are anisotropic and 71 are isotropic. To show the presence of anisotropy within this study, apparent thermal conductivity was measured at 5° angles, from 0° to 180°, on a single point for four samples. Samples were rotated on the stage of the scanner, and the scan line began and ended parallel to the foliation. The results for this is shown in Figure 6 and a sinu-

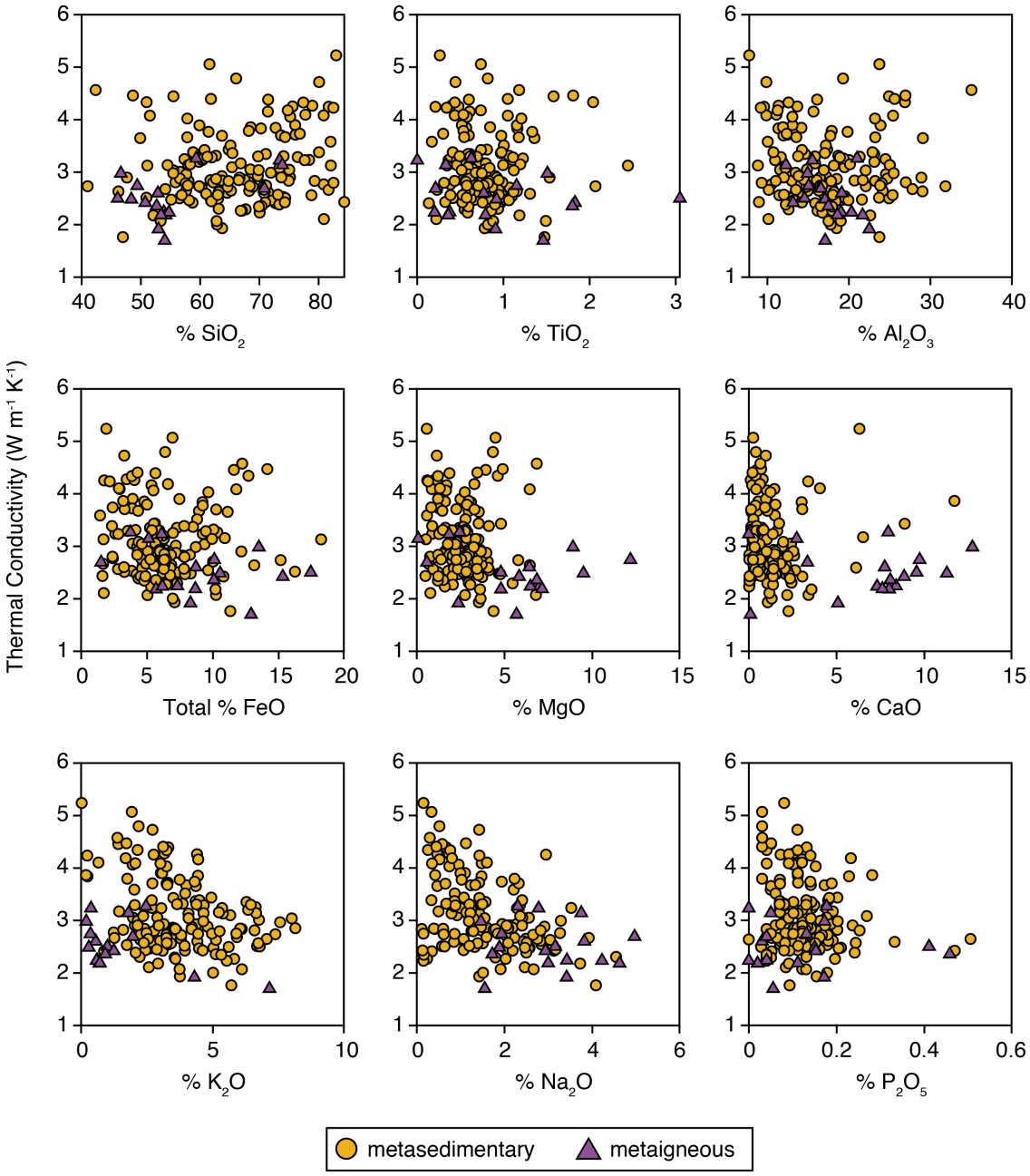

Figure 5: Comparing the k_{geo} values with the major oxide percentages of all the samples.

soidal pattern can be seen, with the starting and finishing conductivity values being similar. In addition to this, each sample has a different magnitude of anisotropy.

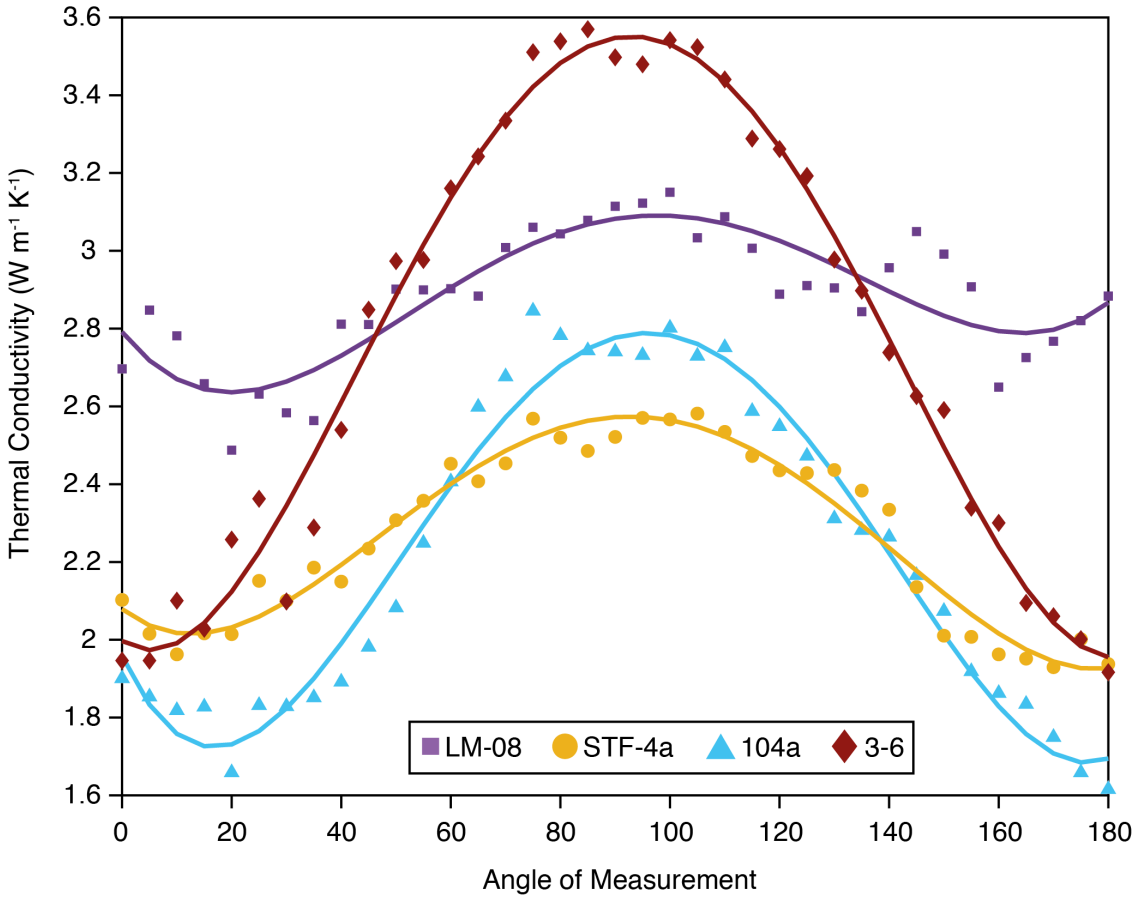

Figure 6: Samples rotated at 5° angles for thermal conductivity measurements. The data shows there is a sinusoidal cycle, which represents anisotropy. The anisotropic values (A) for the samples are: LM-08 = 0.560, STF-4a = 0.540, 104a =0.756, 3-6 = 2.730.

The distribution of anisotropy follows a log-normal distribution (Figure 7). The mean (μ) and standard deviation (σ) for the spread of the data is -2.098 and 1.346, respectively. Therefore, the results for the median anisotropy are:

$$A_{50\%} = \exp(\mu) = 0.123 \tag{7}$$

$$\overline{A} = \exp\left(\mu + \frac{\sigma^2}{2}\right) = 0.304 \tag{8}$$

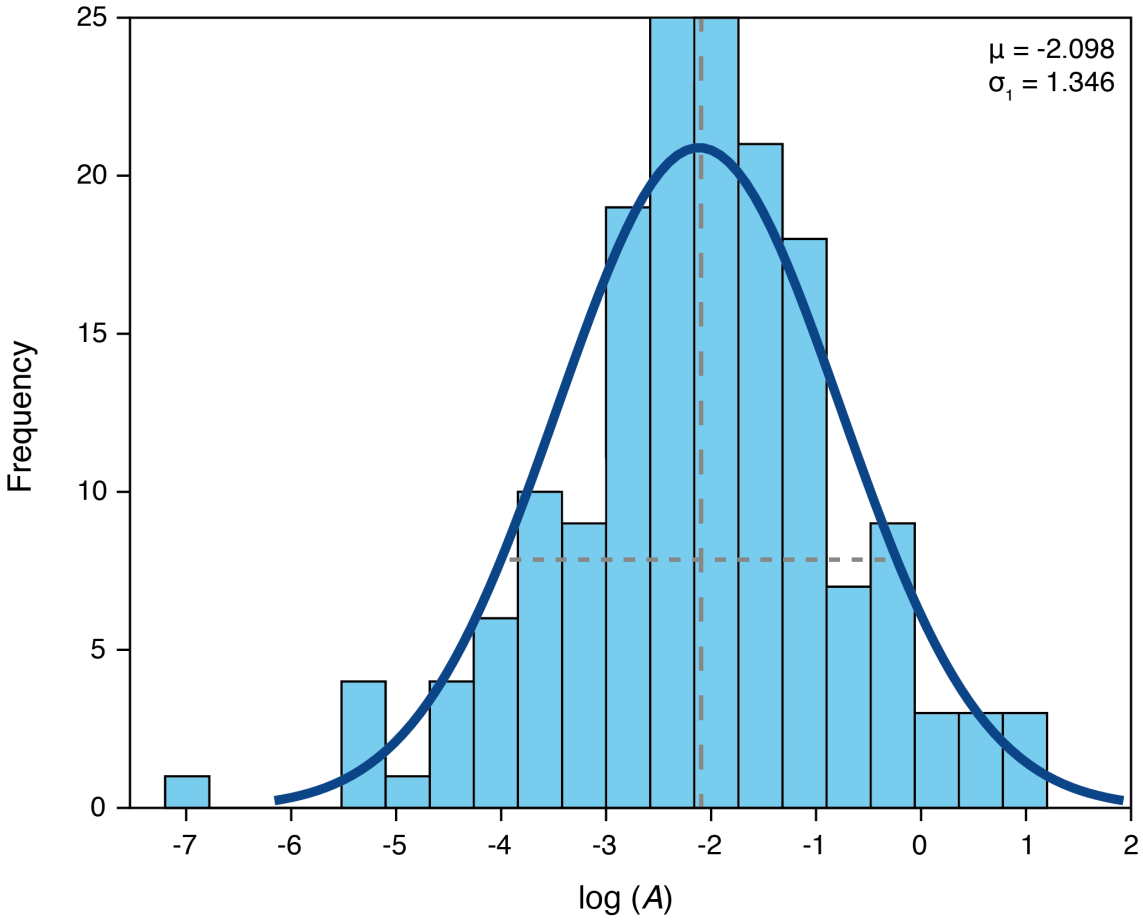

Figure 7: Histogram of anisotropy on log scale.

In addition to the major oxides, thermal conductivity does not have any major correlation with anisotropy for both $k_{\parallel}$ and k_{geo}, with correlation coefficients of 0.144 and -0.221, respectively (Figure 8A and 8C). Although, Figure 8B shows there is a slight negative correlation between $k_{\perp}$ and anisotropy, with a correlation coefficient of -0.566. Most of the data is located ≤ 0.5 for the anisotropic ratio, however $k_{\perp}$ still shows a slight negative trend. Moreover, although $k_{\perp}$ has more correlation than $k_{\parallel}$ and k_{geo}, the correlation is still poor.

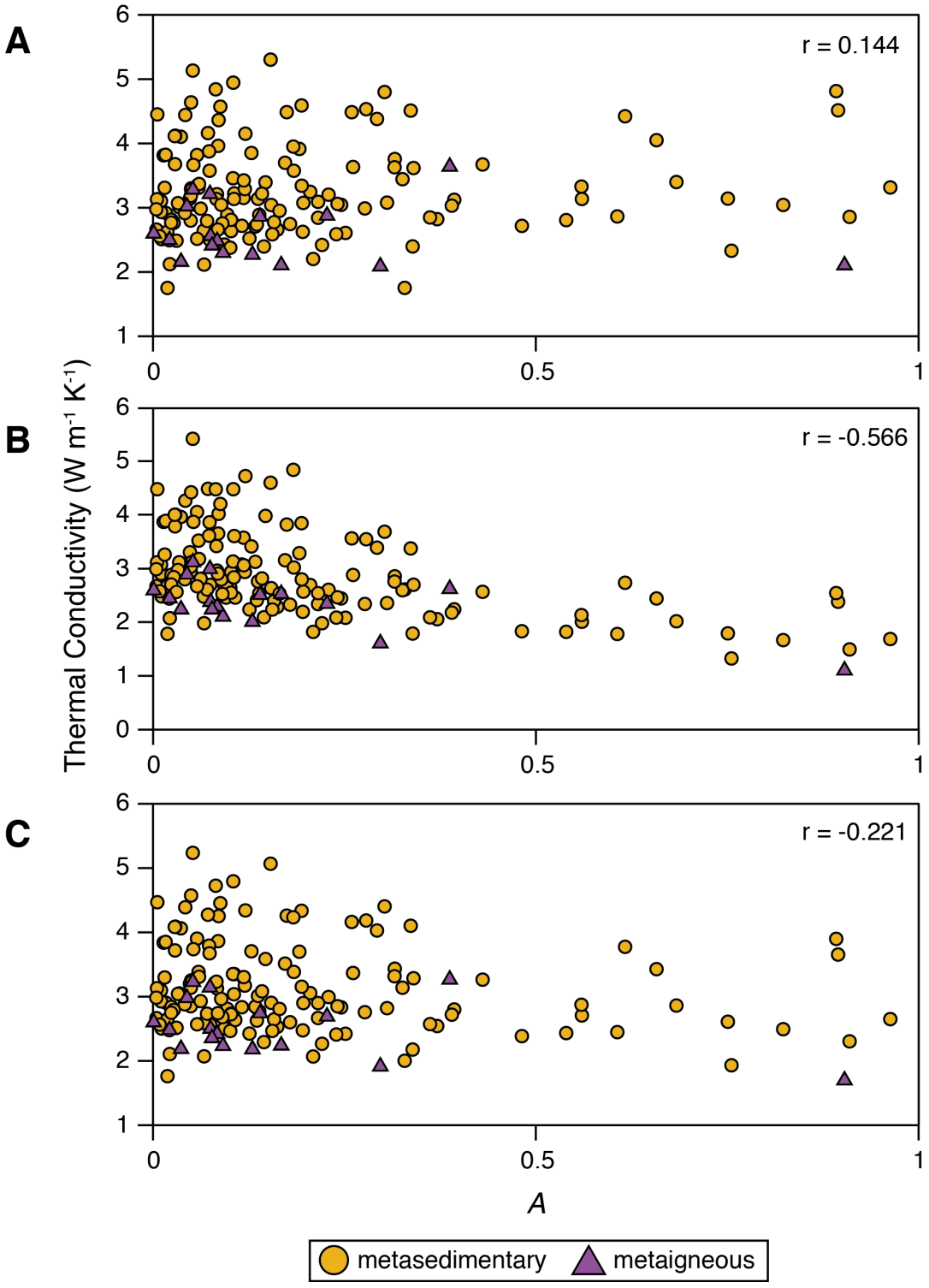

Figure 8: The variation in thermal conductivity and anisotropy. The eight data points above an anisotropy value of 1 have been excluded from this analysis to observe the trend within the bulk of the data. **A**: $k_{\parallel}$ values. **B**: $k_{\perp}$ values. **C**: k_{geo} values.

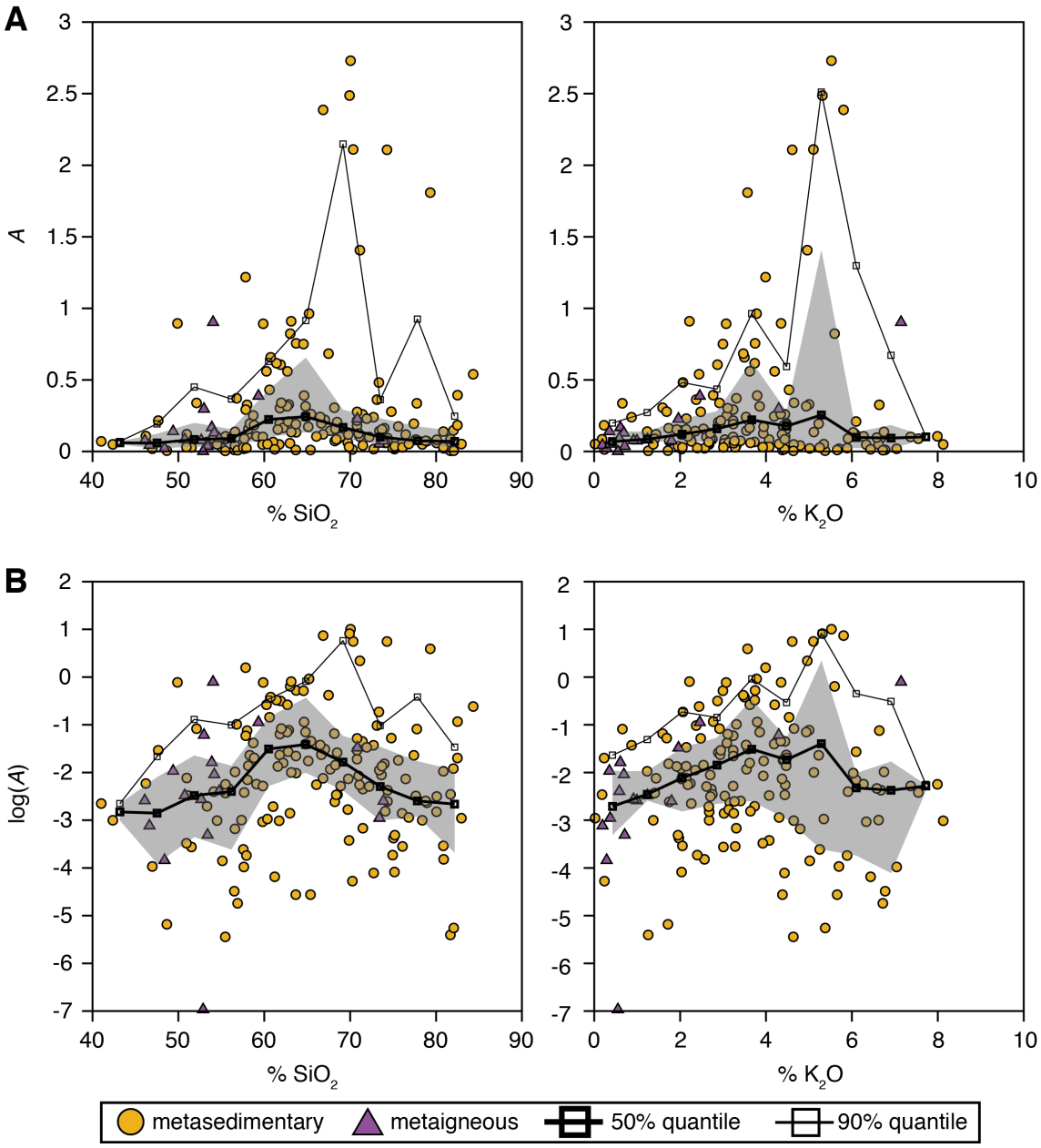

Figure 9: Compositional effects on anisotropy distributions for SiO_2 and K_2O. The shaded region encapsulates the interquartile range. The heavy line identifies 50% quantile and the light line the 90% quantile. **A**: Anisotropy on a linear scale **B**: Anisotropy on the log scale.

Although all major oxides have been compared with anisotropy, only SiO_2 and K_2O produced noteworthy results. For the linear anisotropy values (Figure 9A), the 25%, 50% and 75% quantiles peak between 60% to 65% for SiO_2. On the other hand, the 90% quantile line peaks between 65% to 70% due to five outliers with an anisotropy value ≥ 2. There is another peak between 75% to 80% SiO_2, which is exaggerated by the single outlier above it. These peaks in the 90% quantile require additional data to resolve. K_2O has two peaks which are supported by all the quantiles measured. The first peak is between 3% to 4% K_2O, and the second at approximately 5%. Nevertheless, the overall trend is that as anisotropy increases, K_2O also increases until 5% K_2O, where anisotropy begins to rapidly decrease.

Due to the distribution of anisotropy data on log scale (Figure 7), the oxides are analysed with the anisotropy on log scale (Figure 9B). The SiO_2 figure shows a more prominent peak between 60% to 70% for the 25%, 50% and 75% quantiles. These quantiles incorporate more of the data on log scale than the linear scale. The 90% quantile still defines the same two peaks, however the peaks are lower due to the new distribution of data. The 50%, 75% and 90% quantiles still detect the major peak approximately at 5% K_2O, but for the 25% quantile peaks between 3% to 4% before decreasing rapidly. The first peak which was discerned for the linear values is no longer a prominent peak on log scale.

Density

The measured density values were compared against the calculated density values (data is within Appendix B). The calculated values are modelled from the major oxide geochemistry of the samples (Barette, Poppe, Smets, Benbakkar, & Kervyn, 2016; Bédard et al., 2016; Haus & Pauk, 2010; Slagstad, 2008, 2017). Out of the four compositional groups identified by Hasterok et al. (2018), the samples in this study

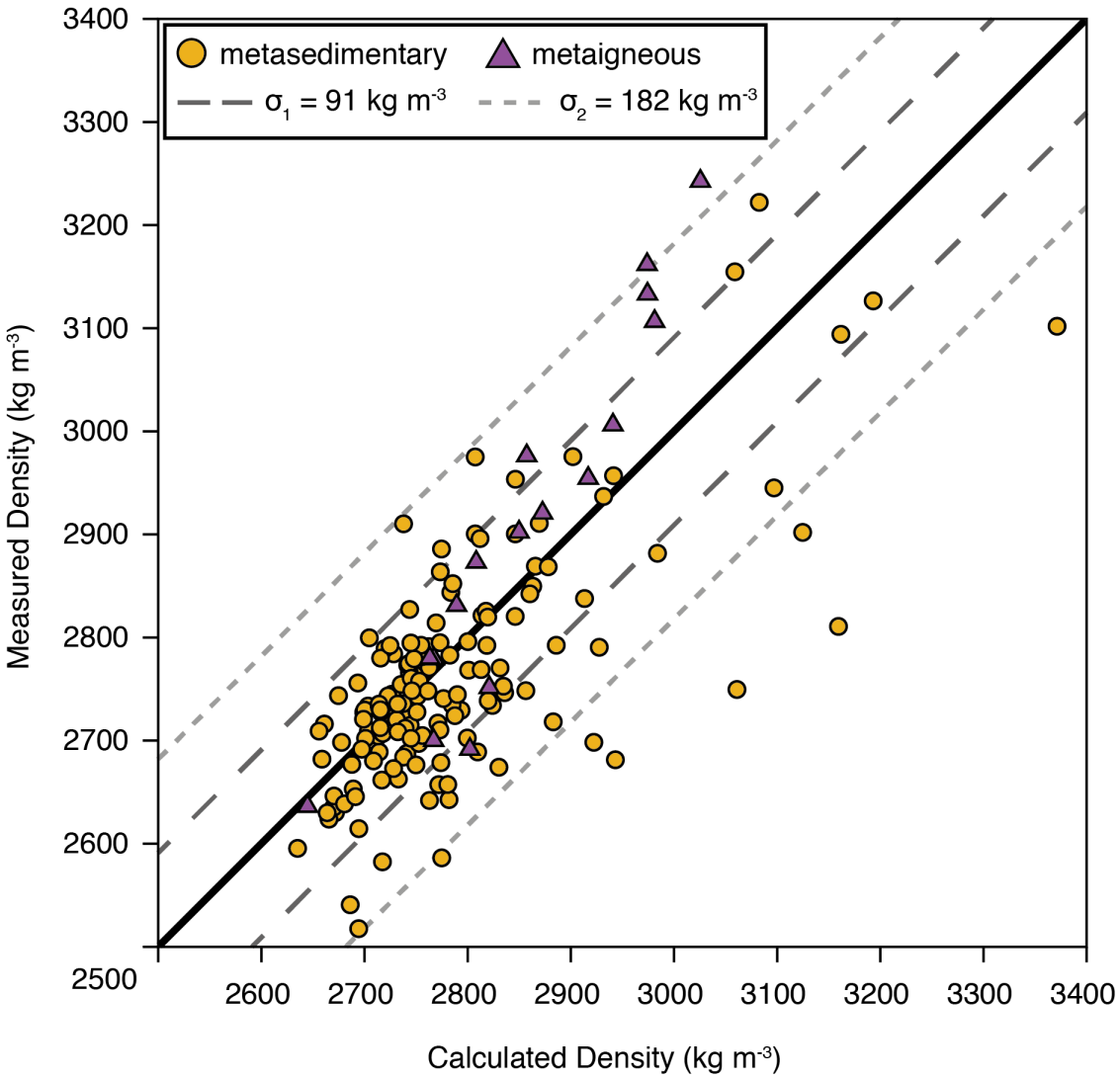

Figure 10: The calculated density values are compares with the measured density values on a 1:1 ratio line (Haus & Pauk, 2010; Barette et al., 2016; Bédard et al., 2016; Slagstad, 2008, 2017).

have been identified as low-Mg silicates. Therefore, the first standard deviation used for the current density model is 91 kg m^{-3}.

DISCUSSION

The initial assumption that composition correlates with thermal conductivity is not established by the data in the present study. From this apparent result, further investigation between all parameters analysed needs to be assessed in detail.

Major oxide geochemistry and mixing models

As discussed in the background, Jennings et al. (2019) showed a relationship exists between thermal conductivity with major oxide composition, mineralogy, P-wave velocity, and density for igneous rocks. In addition to this, conductivity can be indirectly estimated within ±10%, only using the major oxides with the geometric mean (Jennings et al., 2019). It was assumed on the basis of success of the igneous model that a similar result would arise for metamorphic rocks. The proposed method for this study was to use the same mixing models as Jennings et al. (2019) because the models can be easily linearised. However, as stated in the results, there is no clear correlation between conductivity and major oxides (shown in Figure 2 and Figure 5). This lack of correlation includes SiO_2 for which prior studies have suggested is a dominant influence on thermal conductivity (Clauser, 2009, 2011; Clauser & Huenges, 1995; Kukkonen et al., 1999; Pribnow & Umsonst, 1993). It is possible that limiting the study to metasedimentary samples is not sufficient to control the potential influences on conductivity. For the 17 metaigneous samples, there is also no trend with the major oxides. This result is unexpected because of the successful results from Jennings et al. (2019). A feasible reason for the result from this study is the small dataset of the metaigneous rocks.

PRINCIPAL COMPONENTS ANALYSIS

Before attempting to apply the mixing models, PCA was used to explore which major oxides potentially have the most impact on thermal conductivity values, and whether there is correlation between the major oxides and conductivity. As shown in Table 2, $\geq 98\%$ of the explained variance in the results can be described by three principal components. As a result, it seems unlikely that PC4 to PC9 will define a correlation between composition and conductivity. Consequently, if composition does effect conductivity, one or more of the first three components may correlate with conductivity. To determine if there are any composition trend dependencies, vectors of all the oxides were made for each PC, as described in Table 2. Using these values, vectors of the compared components can be plotted (Figure 11), where the larger the vector is, the more influential the major oxide is on conductivity. PC1, PC2 and PC3 were first analysed, however, it is evident there is no trend in conductivity between any of these components. The component showing a possible relationship with conductivity is PC4 (Figure 11). Unfortunately, the variance of PC4 indicates this component is only describing 0.8174% of the data, which is not enough data to analyse the mixing models.

Table 2: The explained variance (Expl. Var.) and vectors for all PC's. When each PC is compared with one another, the two points that make the vector is (0,0) and the two PC's selected for each oxide.

	PC1	**PC2**	**PC3**	**PC4**	**PC5**	**PC6**	**PC7**	**PC8**	**PC9**
Expl. Var.	86.313	9.003	2.824	0.817	0.621	0.337	0.047	0.035	0.003
SiO_2	0.869	0.200	0.040	-0.236	-0.090	-0.062	-0.125	-0.099	0.333
TiO_2	-0.025	-0.032	0.089	-0.008	0.013	-0.052	0.907	-0.231	0.333
Al_2O_3	-0.413	0.626	-0.331	-0.416	-0.059	-0.132	-0.115	-0.097	0.333
FeO (Total)	-0.242	-0.169	0.785	-0.198	0.030	-0.272	-0.252	-0.090	0.333
MgO	-0.114	-0.249	-0.017	-0.128	-0.386	0.793	-0.106	-0.090	0.333
CaO	-0.044	-0.594	-0.486	0.049	-0.206	-0.468	-0.149	-0.113	0.333
K_2O	-0.034	0.334	0.075	0.840	-0.182	-0.022	-0.139	-0.110	0.333
Na_2O	0.003	-0.111	-0.153	0.085	0.874	0.230	-0.137	-0.105	0.333
P_2O_5	0.000	-0.007	-0.002	0.012	0.005	-0.016	0.115	0.936	0.333

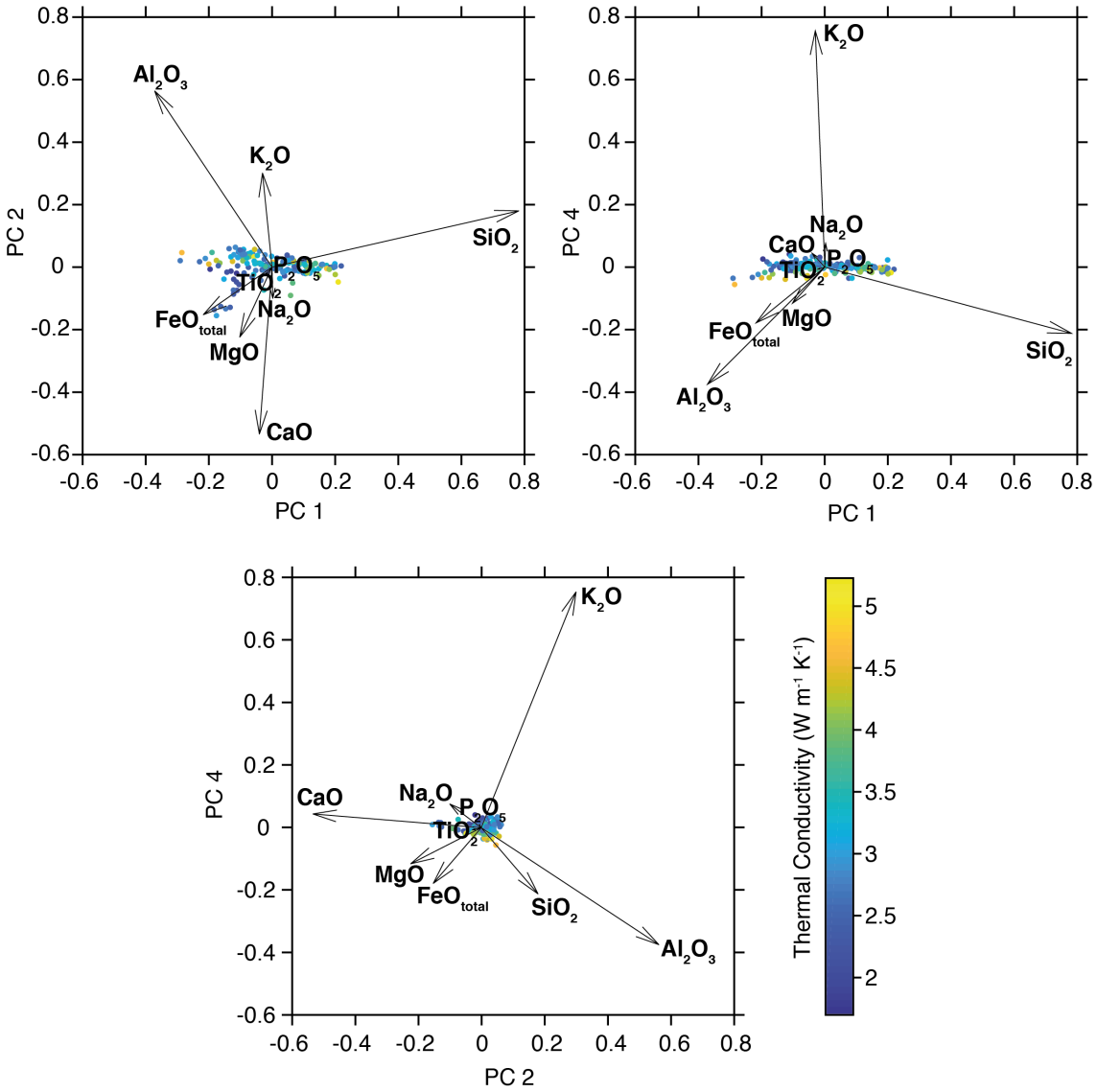

Figure 11: Plotting PC vectors from table 3 with k_{geo} results. **A**: PC1 and PC2. Conductivity values show no trend. **B**: PC1 and PC4. Conductivity values show a trend, increasing downwards. This suggests conductivity increases with Al_2O_3, FeO (Total), SiO_2, and MgO. **C**: PC2 and PC4. Conductivity values show a similar trend to **B**. The same major oxides have an increasing effect on the conductivity.

Table 3: The correlation coefficients of each PC for $k_{\parallel}$, $k_{\perp}$, and k_{geo}.

	PC1	**PC2**	**PC3**	**PC4**	**PC5**	**PC6**	**PC7**	**PC8**	**PC9**
$\boldsymbol{k}_{\parallel}$	0.197	0.216	0.100	-0.458	-0.363	-0.207	0.171	-0.125	0.004
$\boldsymbol{k}_{\perp}$	0.177	0.091	0.003	-0.402	-0.213	-0.163	0.043	-0.010	0.081
$\boldsymbol{k}_{geo}$	0.199	0.169	0.061	-0.483	-0.314	-0.200	0.134	-0.065	0.041

Because a trend was not seen with PC1, PC2, and PC3, more analysis on the components was conducted. The correlation coefficient was calculated for each PC against all thermal conductivity results, and is provided in Table 3. Correlation coefficients vary between 1, a positive correlation, and -1, a negative correlation. When the coefficient is 0, there is no correlation between the selected parameters. For this study, PC4 has the largest correlation with similar values for $k_{\parallel}$, $k_{\perp}$, and k_{geo}, -0.458, -0.402, and -0.483, respectively. Whilst these values are not near 0, they do not indicate there is a strong correlation between PC and conductivity. From this conclusion, the thermal conductivity data produced from this study should not be used with the mixing models because the models will not predict conductivity well.

OTHER CONDUCTIVITY STUDIES ON METAMORPHIC ROCKS

There have been other studies on thermal conductivity with metamorphic rocks. Ray et al. (2015) conducted conductivity measurements on igneous and metamorphic rocks with the optical scanning method and applied four mixing models to determine a relationship between conductivity and mineralogy. The 26 samples varied from charnockites, enderbites, mafic granulites and gneisses within the Southern Granulite Province, India, and are all isotropic to weakly anisotropic. The average conductivity ranges from 2.5 to 3.6 W m^{-1} K^{-1} for charnockites, from 2.5 to 3.6 W m^{-1} K^{-1} for enderbites, from 2.3 to 2.8 W m^{-1} K^{-1} for mafic granulites, and from 2.3 to 3.1 W m^{-1} K^{-1} for gneisses. The mixing model producing the best results for predicting conductivity is the harmonic mean, with a mean deviation of -1 $\pm$ 6%.

The anisotropy values were almost isotropic, hence anisotropy is negligible for the study.

The difference between the study by Ray et al. (2015) and the present study is that all samples are from one province and half of the samples types in the study are igneous rocks. Therefore, when observing the difference between the studies, issues that could have caused the low correlation in the results may be due to the variety of sample locations in the present study. The sample location may have an impact on results because there are many different processes rocks can undergo to become metamorphic (for example contact and regional metamorphism), and all have different P-T conditions (Kelsey & Hand, 2015; Schön, 2015a). These processes would influence porosity, mineralogy, degree of crystallisation and grain orientation, which all impacts conductivity. Additionally, the favourable results produced by Ray et al. (2015) may be assisted by the number of igneous rocks within the study. As discussed earlier, Jennings et al. (2019) created a successful model for plutonic rocks, consequently the results from Ray et al. (2015) may be influenced by the charnockites and enderbites, which are igneous in origin. Furthermore, whilst anisotropy was negligible for Ray et al. (2015), anisotropy is prominent in this study (Figure 6). However, the effects of anisotropy are still generally unknown because anisotropy is a complex parameter and whilst it is mentioned and the ratio is calculated, no other analysis is given in other geophysical studies (Clauser, 2009, 2011; Clauser & Huenges, 1995; Popov et al., 2016; Vosteen & Schellschmidt, 2003).

In earlier studies of thermal conductivity on metamorphic rocks, mixing models are not considered, but rather the effects of other parameters on conductivity. Vosteen and Schellschmidt (2003) constrained how temperature of the sample influences conductivity during the measurement between 0°C and 500°C. From the Eastern Alpine across Europe, 118 samples were collected, where approximately half were metamorphic and the other half sedimentary. The relationship confirmed by the study is when sample temperature increases, conductivity decreases which was pre-

viously established by Sass, Lachenbruch, Moses, & Morgan (1992). In this study, the measurement temperature of the samples was kept constant at room temperature so temperature did not need to be considered as a variable.

Metamorphic rocks form at variable pressures and temperatures, so perhaps prograde, peak or retrograde P-T conditions need to be incorporated. Jõeleht and Kukkonen (1998) show an observation made with their results that even with a variety of metamorphic pressures, conductivity remains constant. The aim of the study was to relate P-wave velocity and heat production within the Baltic Shield in Finland and Estonia. New thermal conductivity measurements were made on the granulite facies rocks, which consisted of migmatites, metasedimentary, and metaigneous rocks. There was no relationship found between heat production and P-wave velocity within the regional rocks as the correlation coefficient was -0.29. For this study, thermal conductivity was analysed with the provided P-T conditions of numerous samples (see Appendix D) however there was no clear correlation between conductivity and metamorphic temperature, or conductivity and metamorphic pressure. This result supports the conclusion made by Jõeleht and Kukkonen (1998) that metamorphic pressures do not effect thermal conductivity.

Anisotropy

To show the existence of anisotropy within the sample selection, four samples with varying anisotropy values were rotated at 5° angles on the TCS stage and thermal conductivity was measured for each 5° angle at one point on the sample. As shown in Figure 6, there is a sinusoidal pattern with all three samples, where the starting and ending conductivity value being almost identical. The fact that the conductivity values change constantly between 0° and 180° indicates anisotropy is present within the samples. Each sample has a different magnitude which indicates anisotropy can impact the conductivity at various levels for each sample. This sinusoidal pattern

was also shown by Clauser & Huenges (1995) and Davis et al. (2007), where both isotropic and anisotropic samples where measured at every 15° angle. Clauser & Huenges (1995) isotropic sample stayed relatively consistent with the conductivity values and the anisotropic samples in both studies also showed a sinusoidal pattern. In addition to this, the measurements were conducted when the samples were both dry and fully fluid saturated. The results showed the same pattern. However, the saturated samples had a marginally higher conductivity values. The study by Davis et al. (2007) only shows anisotropic samples, but the three samples all show different magnitudes of anisotropy which is also observed within the present study (Figure 6).

Deming (1994) showed a strong inverse correlation between thermal conductivity and anisotropy for sedimentary, metamorphic, quartz-rich and clay-rich rocks. The study also shows if the conductivity value is greater than 4 W m^{-1} K^{-1}, anisotropy becomes negligible. The model produced included factoring in the end-members of minerals, and it is suggested the model could be used to derive a correction for anisotropic effects observed during conductivity measurements (Deming, 1994). However, in a contradicting study, Davis et al. (2007) applied the same model for metasedimentary and igneous rocks and did not produce an inverse correlation. The main difference that may be causing these conflicting results is most of Davis et al. (2007) samples contained carbon and carbonate, which lowers to the conductivity and anisotropy (Schön, 2015b). Nevertheless, numerous samples lie well below the modelled curve developed by Deming (1994).

For this study, Figure 8 compares thermal conductivity with anisotropy and as shown, there is not trend for $k_{\parallel}$ and k_{geo} as the correlation coefficients are 0.144 and -0.221, respectively. However, there is a small negative correlation for $k_{\perp}$ with a correlation coefficient of -0.566. This trend does not have the same gradient produced by Deming (1994), but the similarity is that both produce a negative trend. A possible reason for $k_{\perp}$ developing this trend may be caused by the direction of

measurement. To determine $k_{\perp}$ using the optical scanner, the heat flowing through the sample is along the lines of folaition (see Figure 1B, scan line 2). From this scan line, heat can evenly spread out through the foliation, which is dependent on the anisotropy of the sample. Moreover, the correlation coefficient for $k_{\perp}$, while showing a stronger correlation than $k_{\parallel}$ and k_{geo}, is still weak overall. Therefore the $k_{\perp}$ values only agree with Deming (1994) to an extent. Since there is no trend for $k_{\parallel}$ and k_{geo}, these values agree with Davis et al. (2007). In addition to this, the samples within this study did not contain carbon or carbonate, indicating there are not the same potential issues that Davis et al. (2007) encountered. This result indicates overall, the present study supports Davis et al. (2007) more than Deming (1994).

Another aspect which was analysed with anisotropy are the major oxide composition (Figure 9). All the major oxides were evaluated, although only SiO_2 and K_2O showed a possible relationship. Firstly, examining anisotropy on a linear scale (Figure 9A), SiO_2 has a peak between 60% to 65%, and K_2O peaks at approximately 5%. Both of these peaks are reflected more predominantly on the log scale (Figure 9B). When analysing the SiO_2 peaks on both scales, a low percentage of SiO_2 generally indicates mafic rocks and a high percentage reflects felsic rocks. The mid-range percentages of SiO_2 represent the majority of rock types. Therefore, the end-member rock types of SiO_2 have a considerably low anisotropy, and the large compositional range of rock types to have a range of anisotropy. A similar interpretation can be made for K_2O, however instead of having a low gradient after the peak, anisotropy drops rapidly for high K_2O percentages.

Mineralogy

Without modal mineralogy for most of the samples, end-member compositions of the majority of the minerals identified within the samples are used and analyse the presence of minerals with the conductivity values. For the various combinations

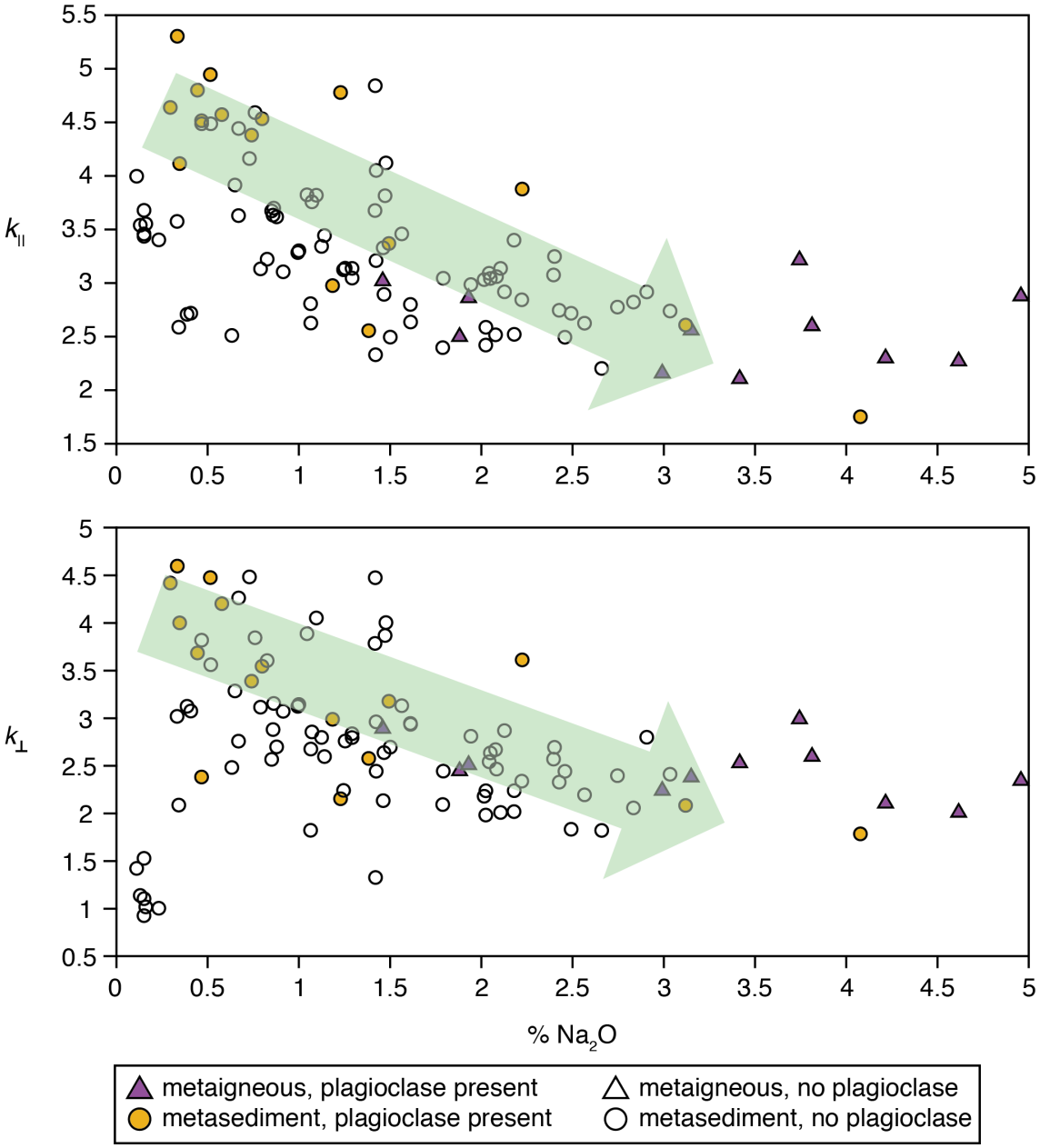

Figure 12: Thermal conductivity of plagioclase bearing samples as a function of Na_2O. Filled points indicate the mineral is present, open points do not indicate mineral presence, and the green arrow indicates the generalised trend.

considered, only plagioclase shows a slight trend and only with Na_2O (Figure 12). A implied trend is used for this analysis as there is an insufficient number of data points. Although this trend is not strong, this does suggest plagioclase has an impact on the thermal conductivity for samples containing Na_2O. The trend in Figure 12 shows as the amount of oxide increases, conductivity decreases. This result suggests mineralogy has an impact that is not clear from major oxide geochemistry on thermal conductivity for metamorphic rocks. It is possible major oxides are well correlated with conductivity for the metaigneous samples because there is a more limited range of mineralogies than found among metamorphic rocks. As a result, a better mineralogic description of metasedimentary samples may be necessary to improve compositional models of thermal conductivity.

Density

As discussed in the results, the majority of the calculated and measured density values lie on and near the 1:1 ratio line and within two standard deviations (Figure 10). This result indicates the propose model developed to indirectly determine density is broadly successful.

While igneous rocks show a systemic thermal conductivity pattern with density (Jennings et al., 2019), our metamorphic samples do not. Jennings et al. (2019) showed conductivity decreases with density until 3000 kg m^{-3}, and above this value, conductivity increases. For metamorphic rocks, density can be related to pressure. When a rock undergoes metamorphism, at peak pressure, porosity is very low and the density increases (Clauser, 1992; Kelsey & Hand, 2015; Schön, 2015a). However, there are no trends between pressure and conductivity in this study, henceforth it is no surprise that density does not correlate with conductivity.

Future considerations

On the basis of this study, several changes are recommended to the sample selection for future studies. From the study, metasedimentary rocks were the primary focus, although perhaps a narrower range of chemistries or rock types within the metasedimentary group needs to be selected, for example, pelites. In addition to this, metaigneous rocks may also be analysed due to the successful results by Jennings et al. (2019). The second aspect to investigate in relation to this the study is to look at many types of provinces, and analyse how the results from the models indirectly calculate thermal conductivity compare or contrast. The results from this consideration would help determine if conductivity models change between different provinces and to see if a conductivity model can be deduced for metamorphic rocks globally.

Metamorphic pressures and temperatures may be a focused study on a single rock type across various P-T conditions. Whilst the results from Jõeleht and Kukkonen (1998) state otherwise, the proposed study has not been focused on a singular rock type. Another factor to consider is mineralogy. As discussed, mineralogy was not conducted on every sample (see Appendix A), therefore a more thorough evaluation could not be made. Jennings et al. (2019) examined CIPW normative mineralogy and modal mineralogy in addition to major oxide geochemistry, which was not as successful as the major oxide model, but still produced meaningful results. From the results of this study, only the present mineralogy produce some sort of a trend, indicating metamorphic rocks rely on this parameter more than the major oxide geochemistry. The mineralogy could also help explain the anisotropy within a sample due to mineral and grain orientation. As discussed in this study, anisotropy can be defined for both lineation and foliation (Vosteen & Schellschmidt, 2003). The two definitions of anisotropy have a different impact on the total conductivity of the sample because aligned sheet silicates have different conductivities compared to randomly orientated ones (Pribnow & Umsonst, 1993).

CONCLUSION

Although a major oxide based compositional model for thermal conductivity was ultimately unsuccessful, there are indications that a mineralogic-based model will be more successful. The results from this study show thermal conductivity ranges between 1.698 and 5.226 W m^{-1} K^{-1}, and the anisotropy ratio ranges from 9×10^{-4} and 2.730, where 0 represents isotropy. From the ratios, 97 samples were classified as anisotropic and 71 samples as isotropic.

Anisotropy showed the most promising results of the study as it produces a log-normal distribution with a mean of -2.098 and standard deviation of 1.347. When analysed with the major oxides, only SiO_2 and K_2O observe a peak in anisotropy between 60 to 65% and 5%, respectively. This peak is further distinguishable by taking the log of anisotropy.

In regards to thermal conductivity with anisotropy, $k_{\parallel}$ and k_{geo} do not show any trends between the two parameters, which is further confirmed by their correlation coefficients of 0.144 and -0.221. However, $k_{\perp}$ shows a negative correlation of -0.566, which supports Deming (1994). Unfortunately, this correlation is still low therefore this study confirms Davis et al. (2007), rather than Deming (1994).

The known mineral assemblages for the samples analysed show a possible negative trend for the presence of plagioclase as a function of Na_2O with $k_{\parallel}$ and $k_{\perp}$. This result indicates as the percentage of Na_2O increases, the thermal conductivity decreases. With this relationship, it is possible with more samples, a more defined trend could be found with plagioclase, along with other minerals.

The calculated density measurements show a promising result as most of the data sits around the 1:1 ratio line, indicating density can be indirectly computed within reasonable values. However, there is no correlation between density and thermal conductivity for metamorphic rocks within this study.

For future studies of determining thermal conductivity indirectly, a narrower range of chemistries or rock types may assist with helping develop a compositionally-based model. This study can be applied to both metasedimentary and metaigneous rocks. From these limitations, it is necessary for future studies to increase the size of the dataset as some trends may be hidden within this study. Another study proposal is to create models that indirectly calculate thermal conductivity for different provinces, and to determine if multiple provinces compare or contrast each other. Furthermore, since there are possible trends within the mineralogy, it is recommended for future considerations that the modal mineralogy would also help develop a model.

ACKNOWLEDGEMENTS

An immense thank you to my supervisor Derrick Hasterok for his ongoing support and never-ending guidance throughout the year. My gratitude goes out to Alicia Pollett and Samuel Jennings for their assistance with the Thermal Conductivity Scanner and providing possible solutions when there was a barrier to overcome. To Martin Hand, whose collaboration to determine the mineralogy in multiple methods was much appreciated. Georgina Gordon and Samuel Williams at the South Australian Drill Core Library are thanked for using the National Virtual Core Library – SA Node. I am grateful to Laura Morrissey, Kiara Alessio, Megan Williams and Mitchell Bockman for providing me with numerous samples, and to Tony Milnes for assistance with locating samples within the crypts at The University of Adelaide.

REFERENCES

ABDULAGATOVA, Z., ABDULAGATOV, I. M., & EMIROV, V. N. (2009). Effect of temperature and pressure on the thermal conductivity of sandstone. International Journal of Rock Mechanics and Mining Sciences, 46(6), 1055-1071. doi:10.1016/j.ijrmms.2009.04.011

BALKAN, E., ERKAN, K., & ŞALK, M. (2017). Thermal conductivity of major rock types in western and central Anatolia regions, Turkey. Journal of Geophysics and Engineering, 14(4), 909-919. doi:10.1088/1742-2140/aa5831

BARETTE, F., POPPE, S., SMETS, B., BENBAKKAR, M., & KERVYN, M. (2016). Spatial variation of volcanic rock geochemistry in the Virunga Volcanic Province: statistical analysis of an integrated database. Journal of African Earth Sciences. doi:10.10.16/j.jafrearsci.2016.09.018

BÉDARD, J.H., HAYES, B., HRYCIUK, M., BEARD, C., WILLIAMSON, N., DELL'ORO, T.A., RAINBIRD, R.H., PRINCE, J., BARAGAR, W.R.A., NABELEK, P.I., WEIS, D., WING, B., SCOATES, J., NASLUND, H.R., COUSENS, B., WILLIAMSON, M.C., HULBERT, L.J., MONTJOIE, R., GIRARD, É., ERNST, R., & LISSENBERG, C.J. (2016). Geochemical database of Franklin sills, Natkusiak basalts and shaler Supergroup rocks, Victoria Island, Northwest Territories, and correlatives from Nunavut and the mainland. Openfile8009. Geological Survey of Canada. doi:10.4095/297842

BECK, J. M., & BECK, A. E. (1965). Computing Thermal Conductivities of rocks from Chips and Conventional Specimens. Journal of Geophysical Research, 70(20), 5227-5239.

BIRCH, F. (1950). Flow of Heat in the Front range, Colorado. Bulletin of hte Geological Society of America, 61, 567-630.

CHOPRA, N., RAY, L., SATYANARAYANAN, M., & ELANGOVAN, R. (2018). Evaluate best-mixing model for estimating thermal conductivity for granitoids from mineralogy: A case study for the granitoids of the Bundelkhand craton, central India. Geothermics, 75, 1-14. doi:10.1016 /j.geothermics.2018.03.011

CLAUSER, C. (1992). Permeability of Crystalline Rocks. Eos Transactions, American Geophysical Union, 73(21), 233-240.

CLAUSER, C. (2009). Heat Transport Processes in the Earth's Crust. Surveys in Geophysics, 30(3), 163-191. doi:10.1007/s10712-009-9058-2

CLAUSER, C. (2011). Thermal Storage and Transport Properties of Rocks, II: Thermal Conductivity and Diffusivity. In Encyclopedia of Solid Earth Geophysics (pp. 1431-1448).

CLAUSER, C., & HUENGES, E. (1995). Thermal Conductivity of rocks and Minerals. In T. J. Ahrens (Ed.), Rock Physics & Phase Relations: A Handbook of Physical Constants (pp. 105-126). AGU Books Board: American Geophysical Union.

CSIRO. (2018, 03/10/2018). HyLogging: saving millions through automated drill core logging. Retrieved from https://www.csiro.au/en/Research/MRF/Areas/Orebody-knowledge/Hylogging

DAVIS, M. G., CHAPMAN, D. S., VAN WAGONER, T. M., & ARMSTRONG, P. A. (2007). Thermal conductivity anisotropy of metasedimentary and igneous rocks. Journal of Geophysical Research, 112(B5). doi:10.1029/2006jb004755

DEMING, D. (1994). Estimation of the thermal conductivity anisotropy of rock with application to the determination of terrestrial heat flow. Journal of Geophysical Research: Solid Earth, 99(B11), 22087-22091. doi:10.1029/ 94jb02164

FUCHS, S., SCHÜTZ, F., FÖRSTER, H.-J., & FÖRSTER, A. (2013). Evaluation of common mixing models for calculating bulk thermal conductivity of sedimentary rocks: Correction charts and new conversion equations. Geothermics, 47, 40-52. doi:10.1016/j.geothermics.2013.02.002

HASTEROK, D., GARD, M., & WEBB, J. (2018). On the radiogenic heat production of metamorphic, igneous, and sedimentary rocks. Geoscience Frontiers, 9(6), 1777-1794. doi:10.1016 /j.gsf.2017.10.012

HAUS, M., & PAUK, T. (2010). Data from the PETROCH lithogeochemical database. Miscellaneous release - data 250. Ontario Geological Survey.

HORAI, K. (1971). Thermal conductivity of rock-forming minerals. Journal of Geophysical Research, 76(5), 1278-1308. doi:10.1029/JB076i005p01278

HORAI, K., & BALDRIDGE, S. (1972a). Thermal Conductivity of Nineteen Igneous rocks, I: Application of the needle probe method to the measurement of the thermal conductivity of rock. Physics of the Earth and Planetary Interiors, 5, 151-156.

HORAI, K., & BALDRIDGE, S. (1972b). Thermal Conductivity of Nineteen Igneous rocks, II: Estimation of the Thermal Conductivity of rock from the mineral and chemical compositions. Physics of the Earth and Planetary Interiors, 5, 157-166.

JENNINGS, S., HASTEROK, D., & PAYNE, J. (2019). A new compositionally-based thermal conductivity model for plutonic rocks. Department of Earth Sciences. University of Adelaide.

JÕELEHT, A., & KUKKONEN, I. T. (1998). Thermal properties of granulite facies rocks in the Precambrian basement of Finland and Estonia. Tectonophysics, 291, 195-203.

KELSEY, D. E., & HAND, M. (2015). On ultrahigh temperature crustal metamorphism: Phase equilibria, trace element thermometry, bulk composition, heat sources, timescales and tectonic settings. Geoscience Frontiers, 6(3), 311-356.

KHANDELWAL, M. (2011). Prediction of thermal conductivity of rocks by soft computing. International Journal of Earth Sciences, 100(6), 1383-1389. doi:10.1007 /s00531-010-0550-1

KUKKONEN, I. T., JOKINEN, J., & SEIPOLD, U. (1999). Temperature and Pressure dependencies of Thermal Transport Properties of Rocks: Implications for uncertainties in Thermal Lithosphere Models and new laboratory measurements of high-grade rocks in the Central Fennoscandian Shield. Surveys in Geophysics, 20, 33-59.

MASON, B. (1952). Principles of Geochemistry. J Wiley & Sons.

POPOV, Y., BEARDSMORE, G., CLAUSER, C., & ROY, S. (2016). ISRM Suggested Methods for Determining Thermal Properties of Rocks from Laboratory Tests at Atmospheric Pressure. Rock Mechanics and Rock Engineering, 49(10), 4179-4207. doi:10.1007/s00603-016-1070-5

POPOV, Y. A. (1983). Noncontact Evaluation of thermal Conductivity of Rocks with the Aid of a Mobile Heat Source. Earth Physics, 19(7), 563-567.

POPOV, Y. A., PRIBNOW, D. F. C., SASS, J. H., WILLIAMS, C. F., & BURKHARDT, H. (1999). Characterization of rock thermal conductivity by high-resolution optical scanning. Geothermics, 28, 253 - 276.

PRIBNOW, D. F. C., & UMSONST, T. (1993). Estimation of Thermal Conductivity from the Mineral Composition: Influence of Frabric and Anisotropy. Geophysical Research Letters, 20(20), 2199-2202.

RAY, L., FÖRSTER, H.-J., FÖRSTER, A., FUCHS, S., NAUMANN, R., & APPELT, O. (2015). Tracking the thermal properties of the lower continental crust: Measured versus calculated thermal conductivity of high-grade metamorphic rocks (Southern Granulite Province, India). Geothermics, 55, 138-149. doi:10.1016/j.geothermics.2015.01.007

RINGNÉR, M. (2008). What is principal component analysis? Nature Biotechnology, 26(3).

SASS, J. H., LACHENBRUCH, A. H., MOSES, T. H., & MORGAN, P. (1992). Heat flow from a scientific research well at Cajon Pass, California. Journal of Geophysical Research, 97(B4). doi:10.1029/91jb01504

SCHÖN, J. H. (2015a). Rocks - Their Classification and General Properties. In J. Cubitt (Ed.), Physical Properties of Rocks: Fundamentals and Principles of Petrophysics (Second ed., pp. 497): Elsevier Science.

SCHÖN, J. H. (2015b). Thermal Properties. In J. Cubitt (Ed.), Physical Properties of Rocks: Fundamentals and Principles of Petrophysics (Second ed., pp. 497): Elsevier Science.

SLAGSTAD, T. (2008). Radiogenic heat production of Archean to Permian geological provinces in Norway. Norwegian Journal of Geology 88, 149e166.

SLAGSTAD, T. (2017). LITO Database (Online): Geochemical Mapping of Norwegian Bedrock. Technical Report. Norges Geologiske Undersøkele (NGU). URL: http://www.ngu.no/lito.

SHLENS, J. (2014). A Tutorial on Principal Component Analysis. 3.02, 1-12.

TUREKIAN, K. (1969). The oceans, streams and atmosphere. In: Handbook of Geochemistry, vol. 1. Springer-Verlag Berlin, Heidelberg, New York, pp. 297-323.

VOSTEEN, H.-D., & SCHELLSCHMIDT, R. (2003). Influence of temperature on thermal conductivity, thermal capacity and thermal diffusivity for different types of rock. Physics and

Chemistry of the Earth, Parts A/B/C, 28(9-11), 499-509. doi:10.1016/s1474-7065(03)00069-x

WOLD, S., ESBENSEN, K., & GELADI, P. (1987). Principal Components Analysis. Chemometrics and Intelligent Labratory Systems, 2, 37-52.

APPENDIX A: MODAL MINERALOGY METHODS

In this study, two methods were selected and tried to calculate the percentage of mineralogy for the samples. The two methods are the HyLogger, and pixel counting. However, due to unsatisfactory results and time constraints, neither of these methods and results were included within the study.

HyLogger

The HyLogger was first selected to determine the mineralogy for its quick process (CSIRO, 2018). Jennings et al. (2019) used pointing counting, but it was found to be time consuming, which is similar for the pixel counting which is later discussed. In conjunction with the HyLogger, a program called The Spectral Geologist 8 (TSG 8) is used to process the collected data. The Hylogger collects spectral data from the samples and then from a database, the spectra which is most compatible with the database spectra determines the mineral. All samples were processed with the HyLogger, which is located at the South Australian Drill Core Library.

METHOD

Samples were split into groups, according to their sample name, and placed along a matte black board, which is then placed in the HyLogger tray (Figure 14). The tray moves in all directions to allow multiple scanning lines on each of the samples, and for this method, there are 5 scanning lines. The scanning process was completed twice for each sample: once with the sample names showing to allow for identification, and the second scan for recording the spectra. The spectra recorded falls within two categories: short-wave infra-red (SWIR) and thermal infra-red (TIR).

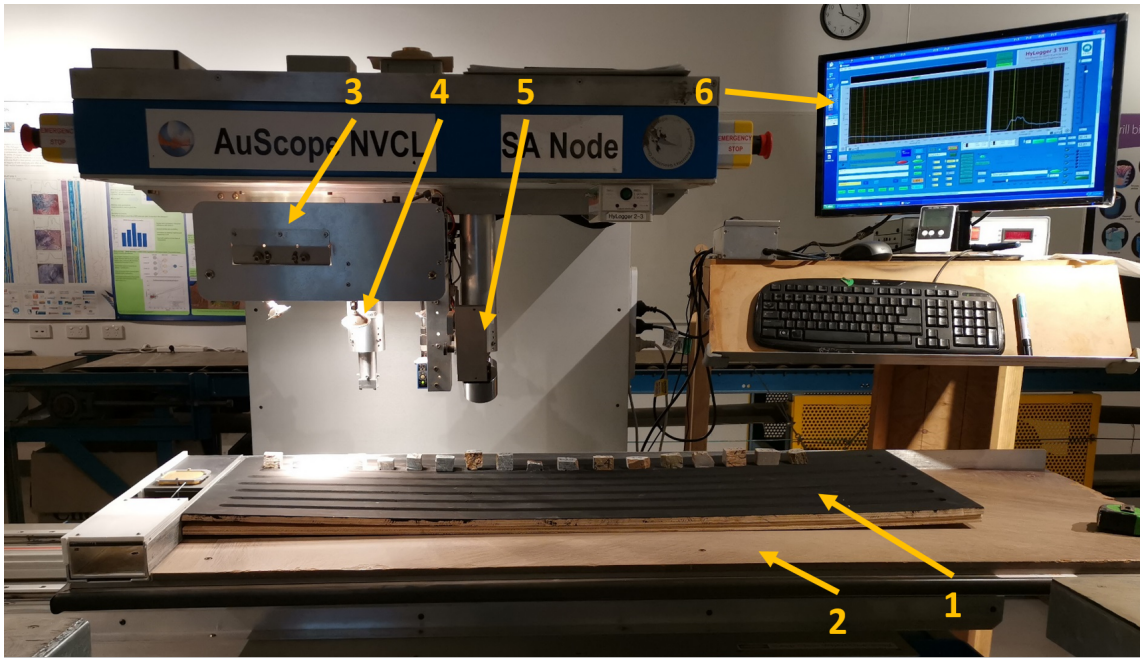

Figure 13: The HyLogger at the South Australian Drill Core Library. **1**: black board to load the samples on. The matte black makes it easier for the camera to pick up all the visual colours of the sample. **2**: HyLogger tray. The tray moves in all directions so the stationary camera can scan multiple areas. **3**: light source. **4**: Hylogger camera. **5**: HyLogger thermal infra-red scanner. **6**: program that collects all raw data from the HyLogger.

To process the spectral data, TSG 8 is used to select and separate all of the samples. Once all samples had been analysed and a final mask had been placed on each group, individual samples were then separated. The method to separate the samples was to locate the final mask on the sample and select only that sample with the class/RockMark edit. The selection was then exported with the appropriate data. To determine the mineralogy, the SWIR data is compared with the SWIR mineral spectra database and the same goes for the TIR data. The spectra that has the most similarities with the database spectra is the mineral that is recorded, along with the second and third most-likely mineral as well.

RESULTS

The HyLogger and TSG 8 produced the results required for the study, as shown in Table 4. The two samples analysed in these results are samples LM-08 (Figure 14A) and COL17-03 (Figure 14B). Due to using TSG 8, all mineralogy is normalised to 100.

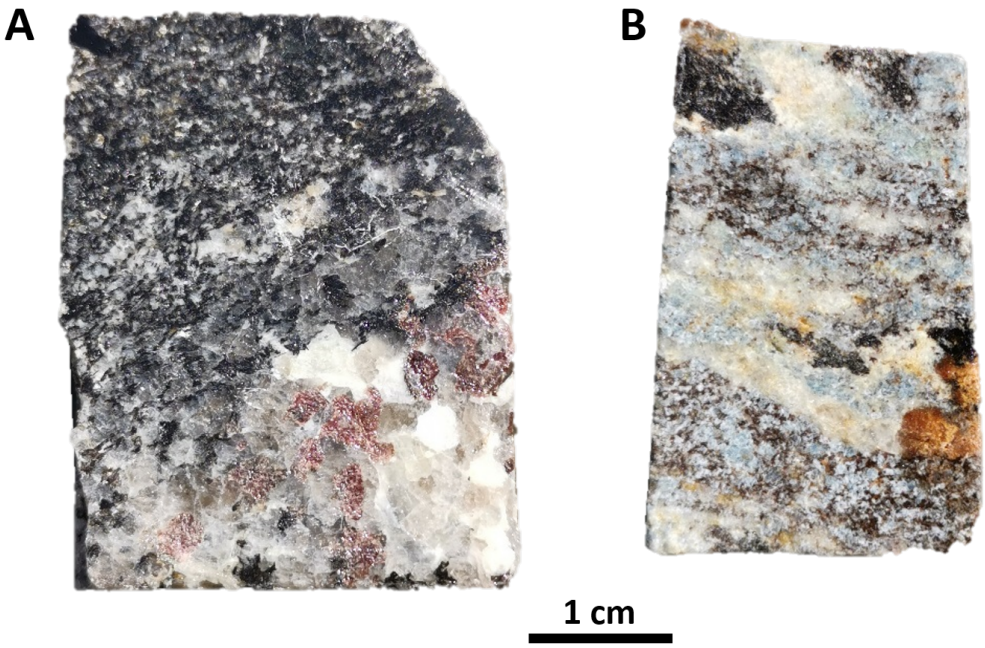

Figure 14: Samples analysed using the HyLogger. For more details on the samples, see Appendix C. **A**: sample LM-08. **B**: sample COL17-03.

Table 4: Results of mineralogy (%) of samples LM-08 and COL17-17 analysed with TSG 8.

	LM-08	**COL17-03**
Quartz	34.614	29.49
Biotite	38.351	
Muscovite	11.649	30.79
Chlorite		32.23
Labradorite	15.386	
Kaolinite		7.50

Figures 15 and 16 display the spectra of with the identified minerals of each sample. For sample LM-08 (Figure 15), although biotite, muscovite, and labradorite do not have a similar comparsion to the database spectra, the TIR spectra is equivalent to quartz. Even though there is a difference in magnitude for both quartz spectra, they show the same general pattern.

Sample COL17-03 shows more comparison with the analysed and database spectra (Figure 16). Muscovite, chlorite, and kaolinite are well identified for the SWIR. The quartz spectra shows some resemblance, but it is not as strong as the other three minerals.

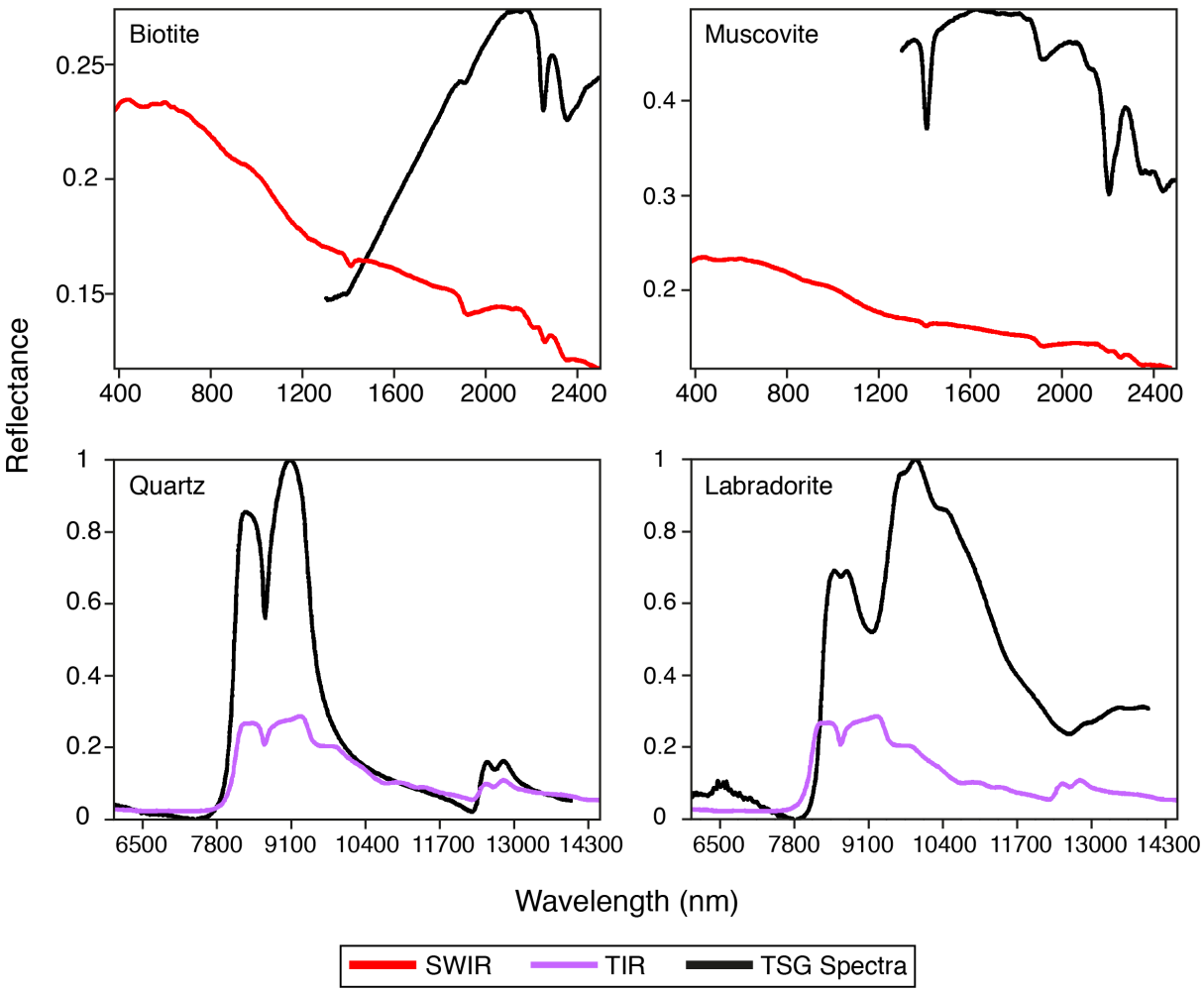

Figure 15: Spectra of sample LM-08 from TSG 8. The database spectra the black line, the SWIR spectra produced by the sample is red, and TIR is purple.

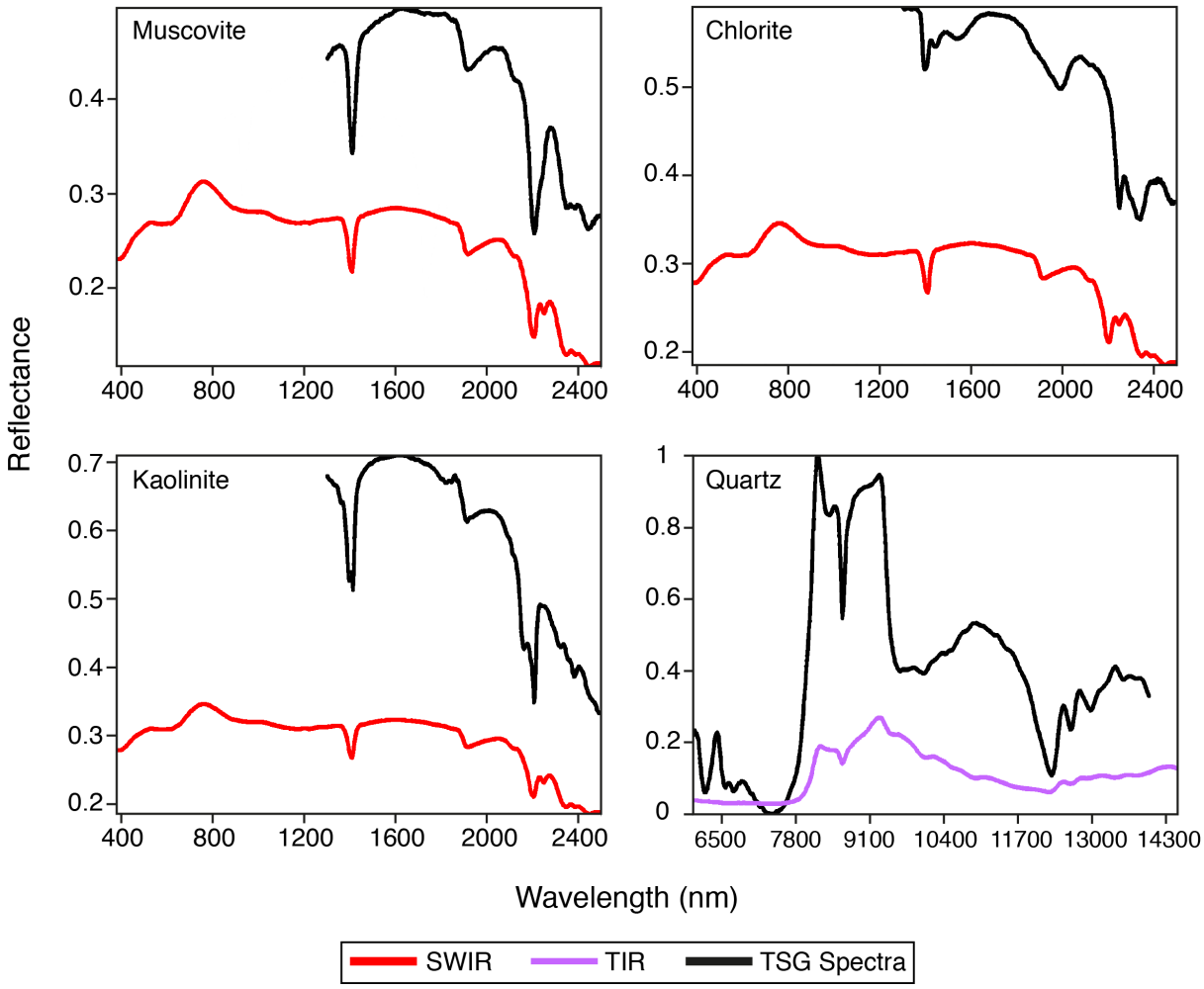

Figure 16: Spectra of sample COL17-13 from TSG 8. The database spectra the black line, the SWIR spectra produced by the sample is red, and TIR is purple.

DISCUSSION

After analysing the minerals present within multiple samples, it was questioned whether or not the HyLogger is an appropriate tool to determine the percentage of mineralogy. Table 5 indicates the minerals present in the samples, and less than half of these minerals were recorded by the HyLogger. For LM-08, there is quartz and biotite in the sample, it does not contain muscovite or labradorite. Furthermore, whilst K-feldspar is similar to labradorite indicating this is what the HyLogger is picking up, it does not explain why garnet is not being identified. The HyLogger is programmed to recognise garnet and the sample contains a visibly

Table 5: Mineralogy confirm by petrography studies (see Appendix F for more details)

	LM-08	**COL17-03**
Quartz	✓	
Biotite	✓	✓
Plagioclase		✓
K-Feldspar	✓	
Garnet	✓	✓
Kyanite		✓

significant amount of garnet, so it is unknown as to why garnet was not interpreted. For COL17-03, none of the mineral assemblage was identified correctly. An excess of muscovite and chlorite was found, most likely misinterpreting the kyanite and biotite. Quartz is identified within the sample, which may have been mistaken for the white plagioclase (Figure 14B). Similar to LM-08, garnet is also not identified.

From these results, it was determined that the data produced from the HyLogger is not sufficient as it does not identify all minerals present within each sample. Whilst there was some similarities with different end-members of a mineral, without knowing the mineralogy beforehand, it is hard to determine the official mineralogy of the sample.

Pixel Counting

Pixel counting was the alternate method suggested after the poor results produced by the HyLogger. This method is best when the mineralogy is known as the method is based on allocating a colour to a mineral. For the mineralogy in this study, past petrological studies were undertaken on most samples, therefore the mineralogy is known (see Appendix F for the mineralogy).

METHOD

Pixel counting can be undertaken within any program that can select pixels by their colour. For this method, Adobe Photoshop was used due to its magic wand tool. Firstly, pictures of the samples were taken with a camera, in sunlight to produce the different colours of the minerals. The image is then uploaded into Adobe Photoshop, with the resolution changed to 300 dpi. With the known mineralogy of the sample, the minerals were selected one at a time by changing the tone, contrast, colour, and hue of the image. To select the desired colour pixels, the magic wand tool is used with a variation on the tolerance. The tolerance determines which other pixels are selected by their colour. Each mineral is then placed in a new layer, and coloured to black so that statistical analysis can be made by selecting all the pixels precisely. The histogram feature in Adobe Photoshop is used to count the number of pixel from the original image and the amount of pixels in the minerals. These results then determine the modal mineralogy by normalising the values to 100%.

RESULTS

Observing Table 6, the number of pixels for each mineral in the 13 samples analysed normalised to calculate the modal mineralogy. The results of the modal mineralogy is shown in Table 7.

DISCUSSION

As shown by the results, the modal mineralogy can be determined accurately, unlike with the HyLogger method. However, there are some issues with the pixel counting method. Firstly, whilst this may be an accurate method, it is not precise as sometimes the magic wand tool will pick up a pixel that is a colour in between two different minerals. In addition to this, it is difficult to differentiate between two

Table 6: The number of pixels for each mineral in the samples analysed.

Sample	Total number of pixels	Number of pixels for each mineral							
		Qtz	Ksp	Pl	Bt	Grt	St	Crd	Ky	Sil
WI-1B	525221	117805			28376	45147		333893		
WI-7	651856	230183	32469	59532	252747	12772		64153		
WI-48	641770	205713	57580	122886	144053	2541		94708		14289
KM-01	511126	173999		138751	85818	24324		88234		
LM-08	1005270	368109	185650		371935	79576				
Col17-3	688338			294089	156740	16735			220774	
Col17-4	470521			159497	243503	8556			46199	12766
Col17-16	647781	34605		119091	235881	126883			131321	
Col17-17	755556	75920		419141	189610	70885				
Col17-21	588340	103548		77341	331830	18410	51685		5526	
Col17-28	750402	87205		105949	464142	64693			28413	
Col17-40	551641	62049		74232	117386	20938			277036	
Col17-48	647850	176996		218667	191414	21175			39598	

Abbreviations: Qtz: quartz, Ksp: K-feldspar, Pl: plagioclase, Bt: biotite, Grt: garnet, St: staurolite, Crd: cordierite, Ky: kyanite, Sil: sillimanite.

Table 7: The modal mineralogy of the samples analysed using the values from Table 6.

Sample	Modal Mineralogy (%)									Total
	Qtz	**Ksp**	**Pl**	**Bt**	**Grt**	**St**	**Crd**	**Ky**	**Sil**	
WI-1B	22.43	0.00	0.00	5.40	8.60	0.00	63.57	0.00	0.00	**100**
WI-7	35.31	4.98	9.13	38.77	1.96	0.00	9.84	0.00	0.00	**100**
WI-48	32.05	8.97	19.15	22.45	0.40	0.00	14.76	0.00	2.23	**100**
KM-01	34.04	0.00	27.15	16.79	4.76	0.00	17.26	0.00	0.00	**100**
LM-08	36.62	18.47	0.00	37.00	7.92	0.00	0.00	0.00	0.00	**100**
Col17-3	0.00	0.00	42.72	22.77	2.43	0.00	0.00	32.07	0.00	**100**
Col17-4	0.00	0.00	33.90	51.75	1.82	0.00	0.00	9.82	2.71	**100**
Col17-16	5.34	0.00	18.38	36.41	19.59	0.00	0.00	20.27	0.00	**100**
Col17-17	10.05	0.00	55.47	25.10	9.38	0.00	0.00	0.00	0.00	**100**
Col17-21	17.60	0.00	13.15	56.40	3.13	8.78	0.00	0.94	0.00	**100**
Col17-28	11.62	0.00	14.12	61.85	8.62	0.00	0.00	3.79	0.00	**100**
Col17-40	11.25	0.00	13.46	21.28	3.80	0.00	0.00	50.22	0.00	**100**
Col17-48	27.32	0.00	33.75	29.55	3.27	0.00	0.00	6.11	0.00	**100**

darker minerals, for example, biotite and orthopyroxene. There is no precise way to create a contrast between two dark minerals, apart from analysing the sample and estimating the amount of biotite and orthopyroxene.

Another aspect that needs to be considered is the method in this study only observes one flat surface of the sample. Therefore, there is only a two dimensional modal mineralogy determined. Since rocks are three dimensional objects, this method needs to be expanded by repeating the process on multiple two dimensional surfaces within the sample, and then an average of the results will be more representative of the three dimensional rock.

However, due to insufficient time, the pixel counting method was discarded so that an attempt at modelling the current data could be undertaken. For future studies determining the modal mineralogy, the three dimensions of the samples need to be included, so the best model may be produced.

APPENDIX B: MEASUREMENT RESULTS

Units of measurement and abbreviations

- Thermal Conductivity (k): W m^{-1} K^{-1}
- Density (ρ): kg m^{-3}
- Parallel thermal conductivity (Equation 2): $k_{\parallel}$
- Perpendicular thermal conductivity (Equation 3): $k_{\perp}$
- Bulk thermal conductivity (Equation 5): k_{geo}
- Anisotropy (Equation 1): α
- Absolute anisotropy (Equation 4): A

Sample	$\boldsymbol{k_{\parallel}}$	$\boldsymbol{k_{\perp}}$	$\boldsymbol{k_{geo}}$	α	$\boldsymbol{A}$	**Measured** ρ	**Calculated** ρ
WI-1B	3.2097	2.9622	3.1250	1.0835	0.0835	2698.34	2922.32
WI-7	2.6082	2.0842	2.4204	1.2514	0.2514	2796.05	2800.18
WI-9	2.5878	2.0879	2.4091	1.2394	0.2394	2810.73	3159.48
WI-48	2.9182	2.8700	2.9021	1.0168	0.0168	2725.71	2731.82
WI-62	3.8151	3.8689	3.8329	0.9861	0.0139	2953.5	2846.31
WI-99	2.3970	2.0937	2.2913	1.1449	0.1449	2770.78	2762.7
KM-01	2.8222	2.0582	2.5403	1.3712	0.3712	2768.32	2800.95
KM-07	2.6250	2.1955	2.4732	1.1956	0.1956	2687.65	2741.15
LM-08	3.1366	2.0104	2.7043	1.5602	0.5602	2768.91	2813.03
104a	2.3307	1.3276	1.9320	1.7556	0.7556	2729.36	2793.6
A325/105b	2.1060	2.5296	2.2387	0.8325	0.1675	2902.32	2849.82
A325/81	2.2704	2.0095	2.1799	1.1298	0.1298	2831.14	2789.27
A325/60	2.2990	2.1065	2.2330	1.0914	0.0914	2873.1	2808.3
A325/148	2.1581	2.2400	2.1851	0.9634	0.0366	2920.78	2872.59
A325/121	2.5996	2.5971	2.5987	1.0009	0.0009	2976.31	2857.28
A325/1105	2.4989	2.4463	2.4812	1.0215	0.0215	3161.82	2973.98
A325/78	3.0193	2.8912	2.9760	1.0443	0.0443	3242.61	3025.6
A325/158	2.8616	2.5106	2.7394	1.1398	0.1398	3106.62	2981.23
A325/1165a	2.8782	2.3453	2.6883	1.2273	0.2273	2636.23	2644.75
A325/1684	2.5593	2.3804	2.4982	1.0752	0.0752	3133.19	2974.32
A325/1687	1.7518	1.7855	1.7629	0.9811	0.0189	2863.68	2773.46
161-2	2.4836	2.2916	2.4179	1.0837	0.0837	3006.2	2940.87
1448	3.2807	3.1183	3.2256	1.0521	0.0521	2751.56	NaN
A222-001	3.2858	3.1301	3.2330	1.0497	0.0497	2630.15	2671.86
A222-002	2.6954	2.4604	2.6147	1.0955	0.0955	2726.44	2719.32
A222-003	3.0434	1.6693	2.4913	1.8232	0.8232	2582.41	2717.43
A222-006	3.1519	3.5747	3.2870	0.8817	0.1183	2695.93	2709.49
A222-007	3.1360	3.4192	3.2277	0.9172	0.0828	2676.92	2687.69
A222-008	2.6588	2.2874	2.5287	1.1624	0.1624	2661.71	2716.81
A222-010	2.8897	2.5375	2.7672	1.1388	0.1388	2614.6	2694.53
A222-011	3.3107	3.5199	3.3790	0.9406	0.0594	2698.3	2677.78
A222-013	1.7529	2.6112	2.0019	0.6713	0.3287	2748.83	2753.6

Sample	$\boldsymbol{k}_{\parallel}$	$\boldsymbol{k}_{\perp}$	$\boldsymbol{k}_{geo}$	α	$\boldsymbol{A}$	**Measured** ρ	**Calculated** ρ
A222-014	3.0111	3.1178	3.0463	0.9658	0.0342	2709.25	2703.84
A222-015	2.1217	2.0761	2.1064	1.0219	0.0219	2635.2	2670.05
A222-016	2.4267	2.6766	2.5073	0.9066	0.0934	2646.23	2670.47
A222-017	3.3951	3.9799	3.5798	0.8531	0.1469	2638.56	2680.55
A222-018	2.1044	1.1057	1.6982	1.9032	0.9032	2691.69	2802.15
A222-019	4.3632	4.0190	4.2453	1.0857	0.0857	2623.82	2665.59
A222-020	2.6592	2.6712	2.6632	0.9955	0.0045	2630	2663.84
A222-021	2.3781	2.6450	2.4639	0.8991	0.1009	2733.51	2703.49
A222-024	2.9342	2.9039	2.9241	1.0105	0.0105	2662.75	2732.85
CHR124	2.7250	2.4606	2.6339	1.1074	0.1074	2749.58	3061.07
STF 1	2.7184	3.0755	2.8326	0.8839	0.1161	2821.38	2813.91
STF-2a	2.7080	3.1256	2.8406	0.8664	0.1336	2717.01	2771.15
STF-2b	2.5107	2.4827	2.5013	1.0112	0.0112	2734.65	2785.01
STF 4a	2.8072	1.8232	2.4311	1.5397	0.5397	2517.56	2694.39
STF-5	3.2228	3.6053	3.3455	0.8939	0.1061	2784.13	2728.29
STF-6	3.3011	3.1441	3.2479	1.0499	0.0499	2789.29	2719.98
STF-8	4.1620	4.4838	4.2666	0.9282	0.0718	2688.97	2714.23
STF-9	2.8946	2.6387	2.8066	1.0970	0.0970	2727.39	2699.3
STF-11	3.8234	3.8875	3.8447	0.9835	0.0165	2704.39	2713.41
STF-12	2.6364	2.9358	2.7327	0.8980	0.1020	2799.67	2704.7
STF-13	3.4587	3.1315	3.3460	1.1045	0.1045	2734.42	2718.28
STF-16a	3.1386	2.7600	3.0069	1.1371	0.1371	2791.2	2762.15
STF-16b	3.1049	3.0728	3.0941	1.0105	0.0105	2743.12	2751.24
STF-17a	4.4868	3.8196	4.2524	1.1747	0.1747	2707.44	2745.82
STF-17b	4.4864	3.5619	4.1543	1.2596	0.2596	2740.77	2776.58
STF-18a	2.8003	2.9453	2.8478	0.9508	0.0492	2716.05	2661.13
STF-18b	3.0463	2.7972	2.9609	1.0891	0.0891	2736.18	2719.95
STF-18c	3.4438	2.5974	3.1347	1.3259	0.3259	2781.24	2755.05
STF-18d	4.4426	4.2631	4.3819	1.0421	0.0421	2734.1	2824.04
STF-20	4.8419	4.4753	4.7165	1.0819	0.0819	2702.22	2701.08
STF-21a	3.8198	4.0528	3.8959	0.9425	0.0575	2684.06	2737.97
STF-21b	4.5911	3.8451	4.3276	1.1940	0.1940	2697.28	2752.65
STF-21c	3.1441	3.3034	3.1963	0.9518	0.0482	2763.87	2748.52
STF-26a	2.8139	2.8830	2.8367	0.9760	0.0240	2674.19	2830.31
STF-26b	4.1040	3.9600	4.0554	1.0364	0.0364	2702.51	2799.68
STF-27	3.6768	3.7856	3.7127	0.9713	0.0287	2727.64	2715.88
STF-28	2.6263	2.6763	2.6429	0.9813	0.0187	2676.45	2749.91
STF-29	4.1207	4.0042	4.0815	1.0291	0.0291	2680.32	2708.76
STF 30	2.9169	2.8005	2.8776	1.0416	0.0416	2827.19	2743.81
STF 31a	2.4953	2.6966	2.5607	0.9254	0.0746	2653.08	2689.13
STF-32	3.1322	3.1160	3.1268	1.0052	0.0052	2595.47	2635.15
ST16-31A	3.1240	2.2419	2.7969	1.3935	0.3935	2645.66	2691.24
IV16-02	2.0872	1.6094	1.9139	1.2969	0.2969	2779.32	2767.35

Sample	$\boldsymbol{k}_{\parallel}$	$\boldsymbol{k}_{\perp}$	$\boldsymbol{k}_{geo}$	α	$\boldsymbol{A}$	**Measured** ρ	**Calculated** ρ
IV16-03A	4.5149	2.3827	3.6486	1.8949	0.8949	2881.67	2984.04
IV16-04	2.6440	2.4797	2.5881	1.0662	0.0662	2792.34	2818.59
IV16-05	3.1420	1.7946	2.6069	1.7508	0.7508	2765.81	2743.54
IV16-06	2.8573	1.4961	2.3030	1.9099	0.9099	2744.96	2726.51
IV16-08	4.7782	2.1544	3.6640	2.2179	1.2179	2869.17	2865.68
IV16-09A	3.2894	2.9372	3.1676	1.1199	0.1199	2825.48	2817.81
IV16-10	4.8141	2.5440	3.8921	1.8924	0.8924	2868.59	2878.07
IV16-11	3.0793	2.3584	2.8174	1.3057	0.3057	2975.1	2807.36
IV16-12	4.3808	3.3892	4.0216	1.2926	0.2926	2975.41	2902.03
IV16-13A	2.1156	1.9832	2.0705	1.0667	0.0667	2900.49	2846.23
IV16-14	2.3980	1.7907	2.1756	1.3391	0.3391	2900.51	2807.39
IV16-15	2.4119	2.2393	2.3529	1.0771	0.0771	2954.47	2916.89
IV16-16	4.5720	4.2025	4.4453	1.0879	0.0879	3094.08	3161.82
IV16-17A	2.7943	2.6101	2.7315	1.0706	0.0706	2901.94	3124.74
IV16-18	4.1514	4.7211	4.3332	0.8793	0.1207	3126.53	3193.14
IV16-21	2.8644	1.7831	2.4458	1.6064	0.6064	2792.48	2754.8
IV16-24	4.4519	4.4770	4.4603	0.9944	0.0056	3222.05	3082.69
IV16-26	4.4230	2.7360	3.7686	1.6166	0.6166	2849.75	2863.09
SQ17-02	3.8519	3.4131	3.6997	1.1285	0.1285	2540.77	2686.17
SQ17-04	3.7577	2.8559	3.4292	1.3158	0.3158	2773.09	2741.95
SQ17-07	3.6387	2.6224	3.2623	1.3876	0.3876	2700.23	2767.06
SQ17-08	4.0508	2.4437	3.4227	1.6577	0.6577	2744.61	2790
SQ17-09	2.9891	2.3413	2.7554	1.2767	0.2767	2729.61	2700.28
SQ17-10	2.4209	1.9831	2.2652	1.2207	0.2207	2727.27	2741.79
SQ17-11	3.3154	1.6889	2.6479	1.9631	0.9631	2910.27	2737.88
SQ17-12	2.7177	1.8340	2.3838	1.4818	0.4818	2706.99	2717.7
SQ17-14	2.7456	2.3287	2.5989	1.1790	0.1790	2681.99	2658.78
SQ17-15	3.9627	3.6519	3.8562	1.0851	0.0851	2819.83	2819.46
SQ17-17	4.5110	3.3750	4.0952	1.3366	0.3366	2720.22	2731.08
SQ17-19	2.7757	2.3967	2.6431	1.1581	0.1581	2735.81	2737.41
SQ17-20	2.8489	2.0919	2.5702	1.3619	0.3619	2712.49	2715.31
SQ17-21	2.8113	2.5514	2.7219	1.1019	0.1019	2780.03	2715.63
SQ17-22	3.2477	2.6946	3.0517	1.2053	0.2053	2754.45	2735.52
SQ17-24	3.2029	2.6055	2.9899	1.2293	0.2293	2720.75	2699.06
SQ17-25	2.4943	2.4424	2.4769	1.0213	0.0213	2794.96	2773.24
SQ17-26	3.2179	2.8170	3.0783	1.1423	0.1423	2732.48	2714.34
SQ17-27	3.3999	2.0193	2.8579	1.6837	0.6837	2774.69	2742.97
SQ17-28	3.0427	2.6357	2.9005	1.1544	0.1544	2743.35	2722.84
SQ17-29	2.5872	2.2383	2.4653	1.1559	0.1559	2843.75	2783.69
SQ17-30	2.9522	2.5336	2.8055	1.1652	0.1652	2760.52	2745.25
SQ17-31	3.3289	2.1344	2.8705	1.5596	0.5596	2852.23	2785.62
SQ17-32	2.9858	2.8109	2.9263	1.0622	0.0622	2714.87	2744.28
SQ17-33	2.8437	2.3394	2.6645	1.2156	0.2156	2735.37	2714.09

Sample	$\boldsymbol{k}_{\parallel}$	$\boldsymbol{k}_{\perp}$	$\boldsymbol{k}_{geo}$	α	$\boldsymbol{A}$	**Measured** ρ	**Calculated** ρ
SQ17-34	2.2028	1.8217	2.0676	1.2092	0.2092	2743.6	2674.81
SQ17-37	2.5212	2.2391	2.4235	1.1260	0.1260	2691.66	2697.37
SQ17-38	3.0320	2.1808	2.7166	1.3903	0.3903	2757.69	2753.24
SQ17-39	3.0752	2.5705	2.8968	1.1964	0.1964	2727.73	2750.86
SQ17-40	3.0450	2.4444	2.8300	1.2457	0.2457	2748.12	2761.5
SQ17-41	2.7389	2.4117	2.6252	1.1357	0.1357	2755.87	2693.55
SQ17-42	3.0597	2.4655	2.8472	1.2410	0.2410	2779.3	2748.08
SQ17-43	2.5168	2.6706	2.5670	0.9424	0.0576	2724.22	2787.68
Col17-3	4.8000	3.6853	4.3953	1.3025	0.3025	2936.81	2931.82
Col17-4	4.9460	4.4768	4.7844	1.1048	0.1048	2956.9	2941.44
Col17-16	4.6390	4.4192	4.5646	1.0497	0.0497	3101.89	3371.37
Col17-17	3.2141	2.9917	3.1382	1.0744	0.0744	2780.06	2763.36
Col17-21	4.5331	3.5459	4.1768	1.2784	0.2784	2820.46	2846.1
Col17-28	4.1149	4.0012	4.0767	1.0284	0.0284	3154.71	3059.05
Col17-40	5.3037	4.5975	5.0570	1.1536	0.1536	2945.1	3096.97
Col17-48	3.8772	3.6126	3.7869	1.0733	0.0733	2814.16	2769.44
1-24	3.9149	3.2866	3.6931	1.1912	0.1912	2837.79	2913.31
1-25	3.6994	3.1553	3.5084	1.1725	0.1725	2746.51	2835.85
2-1	3.6338	2.8810	3.3632	1.2613	0.2613	2738.68	2819.91
2-2	3.2846	3.1250	3.2305	1.0511	0.0511	2895.96	2812
2-3	3.6729	2.5676	3.2597	1.4305	0.4305	2748.44	2856.41
2-5	3.6296	2.7591	3.3125	1.3155	0.3155	2792.47	2885.89
2-7	3.3420	2.7983	3.1500	1.1943	0.1943	2770.48	2831.43
2-17	3.5751	3.0197	3.3794	1.1839	0.1839	2718.21	2882.97
2-18	3.6177	2.6992	3.2812	1.3403	0.3403	2752.73	2834.68
2-19	3.0912	2.5429	2.8964	1.2156	0.2156	2790.51	2927.57
2-20	3.1369	2.8371	3.0336	1.1057	0.1057	2748.37	2745.97
3-4	3.4029	1.0048	2.2660	3.3866	2.3866	2885.84	2774.64
3-5	3.9969	1.4230	2.8328	2.8087	1.8087	2678.6	2774.04
3-6	3.4582	0.9271	2.2299	3.7302	2.7302	2641.94	2763.03
3-9	3.4362	1.1048	2.3541	3.1102	2.1102	2782.86	2782.77
3-14	3.5522	1.0188	2.3426	3.4868	2.4868	2586.24	2774.87
3-17	3.6786	1.5286	2.7451	2.4064	1.4064	2642.77	2781.95
3-24	3.5396	1.1389	2.4255	3.1079	2.1079	2657.3	2772
ST16-1	5.1337	5.4150	5.2258	0.9481	0.0519	2704.87	2756.12
ST16-2A	3.3100	3.2604	3.2934	1.0152	0.0152	2792.19	2724.76
ST16-2B	3.5758	3.8610	3.6684	0.9261	0.0739	2735.54	2732.13
ST16-3A	3.6653	3.8694	3.7321	0.9473	0.0527	2709.22	2656.01
ST16-3B	3.4249	3.0619	3.2994	1.1185	0.1185	2712.05	2739.5
ST16-3C	3.3691	3.1781	3.3042	1.0601	0.0601	2729.94	2715.35
ST16-4	3.0711	2.9741	3.0384	1.0326	0.0326	2708.55	2732.33
ST16-5	2.7562	2.5272	2.6777	1.0906	0.0906	2710.33	2773.14
ST16-9	2.5553	2.5778	2.5628	0.9913	0.0087	2702.22	2745.12

Sample	$\boldsymbol{k}_{\parallel}$	$\boldsymbol{k}_{\perp}$	$\boldsymbol{k}_{geo}$	α	$\boldsymbol{A}$	**Measured** ρ	**Calculated** ρ
ST16-13A	2.7647	2.8414	2.7900	0.9730	0.0270	2688.98	2809.68
ST16-14	2.7681	2.7038	2.7465	1.0238	0.0238	2794.68	2745.02
ST16-15	2.4870	2.5658	2.5130	0.9693	0.0307	2681.4	2943.2
ST16-16A	3.9509	4.8375	4.2267	0.8167	0.1833	2672.84	2728.22
ST16-17	2.6597	2.9058	2.7393	0.9153	0.0847	2657.41	2780.71
ST16-18	3.1854	3.0355	3.1346	1.0494	0.0494	2910.69	2869.44
ST16-19A	2.9760	2.9889	2.9803	0.9957	0.0043	2842.37	2860.34

APPENDIX C: SAMPLE LIST

All samples used in this study have been previously analysed in other studies at the University of Adelaide in past Honours and PhD theses. Details on the various locations, rock type, P-T conditions (Appendix D), geochemistry (Appendix E) and mineralogy (Appendix F) have been received via personal communications, and their corresponding theses.

The references are:

1. MORRISSEY, L. J., HAND, M., & KELSEY, D. E. (2016) A curious case of agreement between conventional thermobarometry and phase equilibria modelling in granulites: New constraints on P–T estimates in the Antarctica segment of the Musgrave–Albany–Fraser–Wilkes Orogen. Journal of Metamorphic Geology, 35, 1023-1050. doi:10.1111/jmg.12266
2. BOLLENHAGEN, W. J. (1994). The influence of bulk rock MnO on garnet development in metamorphic rocks of andalusite-staurolite grade; Kanmantoo, South Australia. (Bachelor of Science (Hons)), University of Adelaide, Adelaide, SA.
3. COLLERSON, K. D. (1972). High grade metamorphic and structural relationships near Amata, Musgraves Ranges, Central Australia. (Bachelor of Science (Hons)), University of Adelaide, Adelaide, SA.
4. PARKER, A. J. (1978). Structural, stratigraphic and metamorphic geology of lower Proterozoic rocks in the Cowell/Cleve district, Eastern Eyre Peninsula. (Bachelor of Science (Hons)), University of Adelaide, Adelaide, SA.
5. DE PRETIS, D. (2009). Application of lithogeochemistry to identify stratigraphic units and provenance of the Kanmantoo group, Kangaroo Island. (Bachelor of Science (Hons)), University of Adelaide, Adelaide, SA.
6. WALSH, A. K., KELSEY, D. E., KIRKLAND, C. L., HAND, M., SMITHIES, R. H., CLARK, C., & HOWARD, H. M. (2015). P–T–t evolution of a large, long-lived, ultrahigh-temperature Grenvillian belt in central Australia. Gondwana Research, 28(2), 531-564. doi:10.1016/j.gr.2014.05.012
7. WHITE, R. W., POWELL, R., & CLARKE, G. L. (2003). Prograde metamorphic assemblage evolution during partial melting of metasedimentary rocks at low pressures: migmatites from Mt Stafford, Central Australia. Journal of Petrology, 44(11), 1937-1960.
8. REDLER, C., JOHNSON, T., WHITE, R. W., & KUNZ, B. (2012). Phase equilibrium constraints on a deep crustal metamorphic field gradient: metapelitic rocks from the Ivrea Zone (NW Italy). Journal of Metamorphic Geology, 30(3), 235-254.
9. BÜTTNER, S. H., GLODNY, J., LUCASSEN, F., WEMMER, K., ERDMANN, S., HANDLER, R., & FRANZ, G. (2005). Ordovician metamorphism and plutonism in the Sierra de Quilmes metamorphic complex: Implications

for the tectonic setting of the northern Sierras Pampeanas (NW Argentina). Lithos, 83(1–2), 143-181. doi: http://dx.doi.org/10.1016/j.lithos.2005.01.006

10. BOCKMANN, M. J. (2017). Crustal thickening in the early Mesoarchaean? Insight from ancient high-pressure metamorphism in SW India. (Bachelor of Science (Hons)), University of Adelaide, Adelaide, SA.
11. BOCKMANN, K. L. (2015). From greenschist to granulite: A mineral equilibria approach to melting and melt loss. (Bachelor of Science (Hons)), University of Adelaide, Adelaide, SA.

Sample	Reference	Rock Type	Rock Origin	Zone	Easting	Northing
WI-1B	1	pelite	metasediment	49D	476974	2648513
WI-7	1	pelite	metasediment	49D	482148	2655814
WI-9	1	migmatitic pelite	metasediment	49D	482319	2655802
WI-48	1	pelite	metasediment	49D	479269	2651203
WI-62	1	felsic gneiss	metasediment	49D	482954	2634764
WI-99	1	pelite	metasediment	49D	478471	2647881
KM-01	1	gneiss	metasediment	49D	483909	2638514
KM-07	1	pelite	metasediment	49D	483909	2638514
LM-08	1	gneiss	metasediment	49D	484460	2654517
104a	2	metapelite	metasediment			
A325/105b	3	mafic granulite	metaigneous			
A325/81	3	mafic granulite	metaigneous			
A325/60	3	mafic granulite	metaigneous			
A325/148	3	mafic granulite	metaigneous			
A325/121	3	mafic granulite	metaigneous			
A325/1105	3	mafic granulite	metaigneous			
A325/78	3	mafic granulite	metaigneous			
A325/158	3	mafic granulite	metaigneous			
A325/1165a	3	quartzo-feldspathic granulite	metaigneous			
A325/1684	3		metaigneous			
A325/1687	3		metasediment			
161-2	4	porphyroblastic amphibolite	metaigneous			
1448	4	migmatite gneiss	metaigneous			
A222-001	5	metasandstone	metasediment			
A222-002	5	metasandstone	metasediment			
A222-003	5	shale	metasediment			
A222-006	5	metasandstone	metasediment			
A222-007	5	metasandstone	metasediment			
A222-008	5	metasandstone	metasediment			
A222-010	5	metasandstone	metasediment			
A222-011	5	metasandstone	metasediment			
A222-013	5	metagreywacke	metasediment			
A222-014	5	metagreywacke	metasediment			
A222-015	5	metasandstone	metasediment			
A222-016	5	metasandstone	metasediment			
A222-017	5	metasandstone	metasediment			
A222-018	5	phyllite	metaigneous			
A222-019	5	metasandstone	metasediment			
A222-020	5	metasandstone	metasediment			
A222-021	5	metagreywacke	metasediment	52J	363718	7112335

Sample	Reference	Rock Type	Rock Origin	Zone	Easting	Northing
A222-024	5	metagreywacke	metasediment	53K	251144	7562280
CHR124	6	metapelite	metasediment	53K	251197	7562283
STF 1	7	hornfel	metasediment	53K	251197	7562283
STF-2a	7	hornfel	metasediment	53K	251292	7562338
STF-2b	7	hornfel	metasediment	53K	251489	7562609
STF 4a	7	schist	metasediment	53K	251909	7562824
STF-5	7	granofel	metasediment	53K	251917	7563411
STF-6	7	granofel	metasediment	53K	252042	7563491
STF-8	7	granofel	metasediment	53K	252321	7563936
STF-9	7	granofel	metasediment	53K	252343	7564021
STF-11	7	granofel	metasediment	53K	252343	7564021
STF-12	7	schist	metasediment	53K	252677	7564418
STF-13	7	schist	metasediment	53K	252677	7564418
STF-16a	7	schist	metasediment	53K	252677	7564418
STF-16b	7	schist	metasediment	53K	252677	7564418
STF-17a	7	psammite	metasediment	53K	253577	7564417
STF-17b	7	psammite	metasediment	53K	253577	7564417
STF-18a	7	leucosome	metasediment	53K	253577	7564417
STF-18b	7	gneiss	metasediment			
STF-18c	7	gneiss	metasediment	53K	254680	7565053
STF-18d	7	gneiss	metasediment	53K	254335	7565037
STF-20	7	schist	metasediment	53K	254335	7565037
STF-21a	7	gneiss	metasediment	53K	254335	7565037
STF-21b	7	gneiss	metasediment	53K	260269	7563397
STF-21c	7	leucosome	metasediment	53K	260269	7563397
STF-26a	7	migmatite	metasediment	53K	260230	7563459
STF-26b	7	migmatite	metasediment	53K	260116	7563459
STF-27	7	gneiss	metasediment	53K	260031	7563436
STF-28	7	gneiss	metasediment	53K	260031	7563436
STF-29	7	quartzite	metasediment	53K	246946	7562150
STF 30	7	gneiss	metasediment	53K	247181	7562335
STF 31a	7	schist	metasediment	53K	241394	7567785
STF-32	7	quartzite	metasediment			
ST16-31A	7	qz-mu schist	metasediment	53K	241394	7567785
IV16-02	8	schist	metaigneous	32T	449812	5083630
IV16-03A	8	schist	metasediment	32T	450804	5083388
IV16-04	8	schist	metasediment	32T	451834	5083247
IV16-05	8	schist	metasediment	32T	452131	5082826
IV16-06	8	schist	metasediment	32T	452387	5082544
IV16-08	8	schist	metasediment	32T	446706	5084125
IV16-09A	8	schist	metasediment	32T	446472	5084856
IV16-10	8	schist	metasediment	32T	445772	5085044
IV16-11	8	schist	metasediment	32T	445135	5086576
IV16-12	8	gneiss	metasediment	32T	445135	5086576

Sample	Reference	Rock Type	Rock Origin	Zone	Easting	Northing
IV16-13A	8	residuum	metasediment	32T	445420	5085449
IV16-14	8	residuum	metasediment	32T	445420	5085449
IV16-15	8	gneiss	metaigneous	32T	444335	5087460
IV16-16	8	gneiss	metasediment	32T	442972	5087044
IV16-17A	8	gneiss	metasediment	32T	443171	5086996
IV16-18	8	gneiss	metasediment	32T	444315	5087488
IV16-21	8	gneiss	metasediment	32T	442203	5073338
IV16-24	8	gneiss	metasediment	32T	435814	5081125
IV16-26	8	schist	metasediment	32T	444484	5072489
SQ17-02	9	schist	metasediment	19J	797518	7122686
SQ17-04	9	schist	metasediment	19J	798565	7123522
SQ17-07	9	slate	metaigneous	19J	796781	7135574
SQ17-08	9	quartzite	metasediment	19J	796781	7135574
SQ17-09	9	schist	metasediment	20J	201717	7105930
SQ17-10	9	schist	metasediment	20J	201717	7105930
SQ17-11	9		metasediment			
SQ17-12	9	schist	metasediment	20J	201948	7106562
SQ17-14	9	gneiss	metasediment	19J	796951	7086142
SQ17-15	9	gneiss	metasediment	19J	796952	7086144
SQ17-17	9	migmatite	metasediment	19J	796959	7086394
SQ17-19	9	migmatite	metasediment	20J	200717	7097754
SQ17-20	9	migmatite	metasediment	20J	200717	7097754
SQ17-21	9	migmatite	metasediment	20J	200717	7097754
SQ17-22	9	migmatite	metasediment	20J	201457	7097766
SQ17-24	9	schist	metasediment	20J	204059	7105244
SQ17-25	9	pelite	metasediment	20J	204059	7105244
SQ17-26	9	schist	metasediment	20J	203787	7096512
SQ17-27	9	pelite	metasediment	20J	203787	7096512
SQ17-28	9	gneiss	metasediment	20J	204883	7096382
SQ17-29	9	gneiss	metasediment	20J	204883	7096382
SQ17-30	9	migmatite	metasediment	20J	204883	7096382
SQ17-31	9	schist	metasediment	19J	795978	7096431
SQ17-32	9	leucosome	metasediment	19J	796473	7096431
SQ17-33	9	migmatite	metasediment	19J	796997	7087473
SQ17-34	9	migmatite	metasediment	19J	797118	7087870
SQ17-37	9	migmatite	metasediment			
SQ17-38	9	migmatite	metasediment			
SQ17-39	9	leucosome	metasediment	19J	796725	7108375
SQ17-40	9	schist	metasediment	19J	796725	7108375
SQ17-41	9	gneiss	metasediment			
SQ17-42	9	gneiss	metasediment			
SQ17-43	9	gneiss	metasediment			
Col17-3	10	schist	metasediment	43N	580150	1372168
Col17-4	10	gneiss	metasediment	43N	579428	1372234

Sample	Reference	Rock Type	Rock Origin	Zone	Easting	Northing
Col17-16	10	metapelite	metasediment	43P	568474	1377081
Col17-17	10	metametaigneous	metaigneous	43P	568474	1377081
Col17-21	10	schist	metasediment	43N	549501	1384129
Col17-28	10	gneiss	metasediment	43N	575714	1366276
Col17-40	10	schist	metasediment	43N	588972	1364575
Col17-48	10	gneiss	metasediment	43N	586884	1369721
1-24	11	pelite	metasediment	53K	277437	7528253
1-25	11	pelite	metasediment	53K	277437	7528253
2-1	11	pelite	metasediment	53K	304533	7508073
2-2	11	pelite	metasediment	53K	304533	7508073
2-3	11	pelite	metasediment	53K	304533	7508073
2-5	11	pelite	metasediment	53K	304533	7508073
2-7	11	pelite	metasediment	53K	304533	7508073
2-17	11	pelite	metasediment	53K	304533	7508073
2-18	11	pelite	metasediment	53K	304533	7508073
2-19	11	pelite	metasediment	53K	304533	7508073
2-20	11	pelite	metasediment	53K	304533	7508073
3-4	11	pelite	metasediment	53K	282331	7522567
3-5	11	pelite	metasediment	53K	282331	7522567
3-6	11	pelite	metasediment	53K	282331	7522567
3-9	11	pelite	metasediment	53K	282331	7522567
3-14	11	pelite	metasediment	53K	282331	7522567
3-17	11	pelite	metasediment	53K	282331	7522567
3-24	11	pelite	metasediment	53K	282331	7522567
ST16-1	7	psammite/qzite	metasediment	53K	258537	7566097
ST16-2A	7	pelite	metasediment	53K	258538	7566097
ST16-2B	7	pelite 1 melt	metasediment	53K	258539	7566097
ST16-3A	7	melt	metasediment	53K	258476	7565983
ST16-3B	7	fg bi-bearing melt	metasediment	53K	258476	7565983
ST16-3C	7	melt	metasediment	53K	258476	7565983
ST16-4	7	bi-bearing melt	metasediment	53K	258479	7565972
ST16-5	7	pelite	metasediment	53K	258534	7566127
ST16-9	7	psammite	metasediment	53K	259078	7566925
ST16-13A	7	gt-cd-opx rock	metasediment	53K	259976	7564102
ST16-14	7	fmr andalusite rock	metasediment	53K	259362	7563665
ST16-15	7	gt-bearing rock	metasediment	53K	259369	7563298
ST16-16A	7	psammite	metasediment	53K	259320	7563275
ST16-17	7	schleric cd rock	metasediment	53K	258861	7562864
ST16-18	7	gt-cd granulite	metasediment	53K	259139	7563105
ST16-19A	7	gt-bearing residual	metasediment	53K	259976	7564102

APPENDIX D: P-T CONDITIONS

Sample	Pressure (kbar)	Temperature °C	Facies
WI-1B	3.90	805.00	
WI-7	4.80	825.00	
WI-9	4.80	825.00	
WI-48	4.10	865.00	
WI-62	4.80	825.00	
WI-99	4.30	760.00	
KM-01	4.40	745.00	
KM-07	4.40	745.00	
LM-08	4.40	745.00	
104a	4.13	580.00	greenschist
A325/105b	8.50	975.00	granulite
A325/81	8.50	975.00	granulite
A325/60	8.50	975.00	granulite
A325/148	8.50	975.00	granulite
A325/121	8.50	975.00	granulite
A325/1105	8.50	975.00	granulite
A325/78	8.50	975.00	granulite
A325/158	8.50	975.00	granulite
A325/1165a	8.50	975.00	granulite
			amphibolite
A325/1684	4.05	685.00	amphibolite
A325/1687	4.05	685.00	amphibolite
161-2			
1448			
A222-001			
A222-002			
A222-003			
A222-006			
A222-007			
A222-008			
A222-010			
A222-011			
A222-013			
A222-014			
A222-015			
A222-016			phrenite
A222-017			
A222-018			
A222-019			
A222-020			
A222-021			granulite

Sample	Pressure (kbar)	Temperature °C	Facies
A222-024			amphibolite
CHR124	7.00	960.00	amphibolite
STF 1	2.55	625.00	amphibolite
STF-2a	2.55	625.00	amphibolite
STF-2b	2.55	625.00	amphibolite
STF 4a	2.55	625.00	amphibolite
STF-5	2.60	628.75	amphibolite
STF-6	2.58	633.40	amphibolite
STF-8	2.75	637.19	amphibolite
STF-9	2.77	638.13	amphibolite
STF-11	2.77	640.88	amphibolite
STF-12	2.77	640.88	amphibolite
STF-13	2.77	640.88	amphibolite
STF-16a	2.80	642.65	amphibolite
STF-16b	2.80	642.65	amphibolite
STF-17a	2.80	642.65	amphibolite
STF-17b	2.80	642.65	amphibolite
STF-18a	2.85	645.00	amphibolite
STF-18b	2.85	645.00	amphibolite
STF-18c	2.85	645.00	amphibolite
STF-18d	2.85	645.00	amphibolite
STF-20	3.13	686.00	amphibolite
STF-21a	3.06	676.00	amphibolite
STF-21b	3.06	676.00	granulite
STF-21c	3.06	676.00	granulite
STF-26a	3.66	785.71	granulite
STF-26b	3.66	785.71	granulite
STF-27	3.66	785.71	granulite
STF-28	3.66	785.71	granulite
STF-29	3.90	800.00	granulite
STF 30	3.90	800.00	granulite
STF 31a	2.27	602.80	
STF-32	2.30	605.50	
ST16-31A	2.10	590.00	
IV16-02	5.95	690.00	
IV16-03A	5.70	675.00	
IV16-04	7.80	742.50	
IV16-05	7.80	742.50	
IV16-06	7.80	742.50	
IV16-08	8.00	815.00	
IV16-09A	8.00	815.00	
IV16-10	8.20	810.00	
IV16-11	10.35	870.00	
IV16-12	10.35	870.00	

Sample	Pressure (kbar)	Temperature °C	Facies
IV16-13A	8.20	810.00	
IV16-14	8.20	810.00	
IV16-15	9.10	860.00	
IV16-16	9.50	870.00	
IV16-17A	9.50	870.00	
IV16-18	9.10	860.00	
IV16-21	5.70	840.00	
IV16-24	9.50	870.00	greenschist
IV16-26	5.35	830.00	greenschist
SQ17-02	1.00	344.29	greenschist
SQ17-04	1.00	344.29	greenschist
SQ17-07	1.00	344.29	amphibolite
SQ17-08	1.00	344.29	amphibolite
SQ17-09	3.10	535.54	amphibolite
SQ17-10	3.10	535.54	amphibolite
SQ17-11			
SQ17-12	2.75	503.66	
SQ17-14			granulite
SQ17-15			granulite
SQ17-17			granulite
SQ17-19	5.23	729.70	granulite
SQ17-20	5.23	729.70	granulite
SQ17-21	5.23	729.70	amphibolite
SQ17-22			amphibolite
SQ17-24	2.30	462.68	amphibolite
SQ17-25	2.30	462.68	amphibolite
SQ17-26			granulite
SQ17-27	4.30	644.82	granulite
SQ17-28			granulite
SQ17-29			amphibolite
SQ17-30			
SQ17-31			granulite
SQ17-32			granulite
SQ17-33	7.05	854.54	granulite
SQ17-34			granulite
SQ17-37			amphibolite
SQ17-38	4.50	663.04	amphibolite
SQ17-39	4.50	663.04	granulite
SQ17-40	4.50	663.04	granulite
SQ17-41	4.85	694.91	granulite
SQ17-42	4.85	694.91	granulite
SQ17-43	4.85	694.91	granulite
Col17-3	11.70	885.00	granulite
Col17-4	11.70	885.00	granulite

Sample	Pressure (kbar)	Temperature °C	Facies
Col17-16	11.70	885.00	granulite
Col17-17	11.70	885.00	granulite
Col17-21	11.70	885.00	granulite
Col17-28	11.70	885.00	granulite
Col17-40	11.70	885.00	amphibolite
Col17-48	11.70	885.00	amphibolite
1-24	4.00	490.00	granulite
1-25	4.00	490.00	granulite
2-1	3.50	500.00	granulite
2-2	3.50	500.00	granulite
2-3	3.50	500.00	granulite
2-5	3.50	500.00	granulite
2-7	3.50	500.00	granulite
2-17	3.50	500.00	granulite
2-18	3.50	500.00	granulite
2-19	3.50	500.00	amphibolite
2-20	3.50	500.00	amphibolite
3-4	2.50	560.00	amphibolite
3-5	2.50	560.00	amphibolite
3-6	2.50	560.00	amphibolite
3-9	2.50	560.00	amphibolite
3-14	2.50	560.00	amphibolite
3-17	2.50	560.00	
3-24	2.50	560.00	
ST16-1	3.60	780.00	
ST16-2A	3.60	780.00	
ST16-2B	3.60	780.00	
ST16-3A	3.60	780.00	
ST16-3B	3.60	780.00	
ST16-3C	3.60	780.00	
ST16-4	3.60	780.00	
ST16-5	3.60	780.00	
ST16-9	3.70	790.00	
ST16-13A	3.60	780.00	
ST16-14	3.83	789.89	
ST16-15	3.76	779.78	
ST16-16A	3.76	779.78	granulite
ST16-17	3.60	756.19	
ST16-18	3.69	769.67	
ST16-19A	3.60	780.00	

APPENDIX E: MAJOR OXIDE GEOCHEMISTRY

	SiO_2	TiO_2	Al_2O_3	FeO total	MgO	CaO
WI-1B	51.09	2.44	18.15	18.21	3.51	1.02
WI-7	58.72	0.97	16.95	10.8	2.83	3.05
WI-9	72.72	0.13	15.86	6.13	3.72	0.18
WI-48	75.16	0.55	11.83	5.04	1.61	1.59
WI-62	70.26	1.16	11.34	9.21	3.08	3.01
WI-99	67.68	0.55	12.6	7.28	5.45	1.06
KM-01	56.79	1.1	19.51	9.63	4.11	2.64
KM-07	61.79	0.67	19.19	7.21	2.71	1.31
LM-08	60.26	1.07	17.88	10.01	4.04	0.96
104a	63.71	0.78	18.48	7.09	3.53	1.08
A325/105b	53.89	0.38	19.01	7.3	6.97	8.38
A325/81	54.18	0.36	21.68	5.68	4.79	7.99
A325/60	54.75	0.2	20.32	6.16	6.46	7.3
A325/148	53.4	0.79	18.6	8.66	7.13	7.61
A325/121	52.88	0.77	19.11	8.7	6.4	7.74
A325/1105	48.39	0.92	17.07	10.54	9.48	11.27
A325/78	46.64	1.51	14.93	13.49	8.89	12.73
A325/158	49.39	1.15	15.06	10.1	12.16	9.72
A325/1165a	70.84	0.21	16.56	1.51	0.58	3.34
A325/1684	46.09	3.05	14.55	17.43	4.78	9.55
A325/1687	46.97	1.48	23.74	11.32	4.37	2.26
161-2	50.74	1.83	13.14	15.3	5.82	8.84
1448	73.4	0	15.51	6.1	1.84	0
A222-001	78.4	0.36	11.17	2.59	0.88	0.26
A222-002	71.49	0.67	13.61	4.66	2.44	1.69
A222-003	63.02	0.83	19.59	6.2	2.92	0.49
A222-006	76.47	0.49	11.65	3.54	1.7	1.62
A222-007	77.65	0.46	10.94	2.82	1.27	1.37
A222-008	73.98	0.6	12.59	3.83	1.78	2.2
A222-010	80.85	0.38	10.48	2.41	0.9	0.89
A222-011	80.06	0.41	10.73	2.34	0.87	0.33
A222-013	62.85	0.82	17.76	6.95	3.63	1.3
A222-014	75.04	0.58	11.56	3.9	1.82	2.4
A222-015	80.89	0.22	10.12	1.71	0.77	1.17
A222-016	74.35	0.41	13.01	3.28	1.19	0.37
A222-017	82.02	0.17	10.04	1.44	0.58	1.49
A222-018	54.04	1.46	17.09	12.9	5.67	0.09
A222-019	81.69	0.21	9.59	1.74	0.59	0.41
A222-020	81.67	0.23	10.17	1.66	0.67	0.38
A222-021	72.21	0.57	13.24	4.21	2.34	2.11
A222-024	63.67	0.72	17.2	6.39	3.62	1.69
CHR124	46.21	1.15	29.02	13.13	6.43	0.78
STF 1	58.04	0.59	23.21	8.25	2.77	0.49

	SiO_2	TiO_2	Al_2O_3	FeO total	MgO	CaO
STF-2a	63.7	0.6	20.68	6.04	2.17	0.3
STF-2b	56.51	0.62	24.93	7.4	2.65	0.35
STF 4a	84.33	0.32	8.96	1.61	0.49	0.67
STF-5	59.1	0.61	23.1	7.27	2.43	0.25
STF-6	57.35	0.67	24.49	6.97	2.44	0.33
STF-8	78.93	0.39	11.37	3.45	1.06	0.79
STF-9	55.84	0.65	26.98	5.79	2.15	0.38
STF-11	72.74	0.57	14.18	4.79	1.6	0.54
STF-12	59.84	0.58	22.07	6.09	1.99	0.32
STF-13	71.09	0.59	14.61	5.22	1.62	0.75
STF-16a	56.6	0.6	25.2	7.18	2.07	0.21
STF-16b	65.38	0.59	19.46	5.68	1.96	0.22
STF-17a	75.6	0.48	13.67	4.04	1.15	0.11
STF-17b	71.43	0.61	15.66	5.34	1.69	0.19
STF-18a	61.74	0.53	21.71	4.3	1.48	0.36
STF-18b	57.67	0.59	24.55	5.95	2.1	0.19
STF-18c	58	0.46	25.04	6.29	2.1	0.21
STF-18d	71.48	0.6	16.1	5.63	1.86	0.22
STF-20	80.08	0.44	9.87	3.27	1.14	0.97
STF-21a	76.04	0.52	13.08	3.91	1.21	1.01
STF-21b	77.42	0.44	12.59	3.85	1.21	0.4
STF-21c	59.81	0.72	23.12	6.21	2.1	0.34
STF-26a	74.95	0.56	13	6.05	1.86	0.48
STF-26b	75.2	0.58	13.06	5.48	1.66	1.02
STF-27	76.09	0.55	12.44	3.88	1.27	0.95
STF-28	57.63	0.61	24.15	6.83	2.29	0.26
STF-29	80.85	0.44	9.86	2.92	0.85	1.46
STF 30	56.59	0.61	24.71	6.75	2.42	1.09
STF 31a	78.79	0.39	11.46	2.79	0.93	0.63
STF-32	82.06	0.34	8.83	1.7	0.52	0.27
ST16-31A	82.5	0.31	9.3	2.38	0.75	0.64
IV16-02	52.97	0.91	22.51	8.3	2.36	5.07
IV16-03A	49.89	1.36	29.08	11.12	3.53	0.15
IV16-04	61.03	1.31	16.89	6.76	4.06	6.11
IV16-05	64.56	0.79	18.23	5.86	2.82	1.74
IV16-06	63.13	0.94	17.23	6.43	2.95	2.43
IV16-08	57.83	1.18	23.23	8.94	2.95	0.48
IV16-09A	66.85	0.8	15.86	5.81	2.06	6.5
IV16-10	59.88	1.16	23.88	7.45	2.48	0.97
IV16-11	68.16	0.56	15.41	7.71	2.04	2.58
IV16-12	57.84	1.21	23.2	9.65	2.73	1.24
IV16-13A	53.34	1.49	19	10.24	6.78	3.4
IV16-14	52.12	1.19	22.61	10.19	3.6	3.57
IV16-15	52.67	1.8	17.49	10.07	6.83	8.05
IV16-16	55.49	1.58	24.91	11.59	3.92	0.47
IV16-17A	41.02	2.07	31.84	15.14	5.77	1.2

	SiO_2	TiO_2	Al_2O_3	FeO total	MgO	CaO
IV16-18	50.98	2.04	26.87	12.69	4.61	0.38
IV16-21	61.9	0.98	18.37	6.75	3.5	2.31
IV16-24	48.66	1.81	26.94	14.12	4.89	0.7
IV16-26	61.42	1.33	19.84	9.23	2.98	0.37
SQ17-02	73.64	0.6	11.96	3.29	2.25	3.04
SQ17-04	64.81	0.81	17.33	5.6	3.52	1.72
SQ17-07	59.33	0.63	21	3.74	2.44	7.93
SQ17-08	60.74	0.74	14.24	5.51	4.79	8.87
SQ17-09	70.81	0.68	14.07	4.57	2.31	1.74
SQ17-10	67.06	0.86	16.15	5.7	3.05	1.38
SQ17-11	65.21	0.85	16.31	6.33	3.69	1.19
SQ17-12	73.35	0.9	12.26	4.36	1.99	2.35
SQ17-14	70.8	0.56	14.26	3.25	2.15	2.07
SQ17-15	68.52	0.84	11.91	3.19	2.95	11.71
SQ17-17	77.76	0.54	11.11	2.86	1.31	4.05
SQ17-19	68.28	0.9	14.94	5.42	2.54	2.12
SQ17-20	73.12	0.98	12.02	4.62	2.1	2.04
SQ17-21	68.89	0.84	14.81	5.16	2.35	1.9
SQ17-22	68.48	0.78	14.85	5.62	2.84	1.95
SQ17-24	71.93	0.68	13.46	4.25	2.19	1.9
SQ17-25	55.12	1.01	21.6	8.31	4.67	1.6
SQ17-26	73.39	0.84	12.22	4.35	2.25	1.96
SQ17-27	67.48	0.89	14.46	6.47	3.54	1.41
SQ17-28	73.7	0.82	12.01	4.31	2.2	2.53
SQ17-29	58.14	1.06	19.94	7.88	4.76	1.52
SQ17-30	62.2	0.99	17.59	6.59	3.72	2.22
SQ17-31	62.7	0.93	18.51	7.19	3.96	0.93
SQ17-32	69.73	0.91	13.83	5.93	2.94	1.4
SQ17-33	70.8	0.94	13.49	4.92	2.52	1.81
SQ17-34	62.78	0.88	17.5	5.03	2.74	2.18
SQ17-37	70.99	0.76	14.13	4.51	2.02	1.38
SQ17-38	64.64	0.87	17.49	6.22	3.44	1.36
SQ17-39	66.65	0.92	16.45	5.97	2.99	1.51
SQ17-40	64.8	0.83	17.81	6.82	2.8	0.82
SQ17-41	63.14	1.12	18.17	5.53	2.37	1.4
SQ17-42	66.51	0.95	16.06	6.31	2.97	1.48
SQ17-43	62.99	0.95	18.03	7.8	3.42	1.41
Col17-3	61.82	1.05	25.61	4.28	3.44	0.21
Col17-4	66.07	0.82	19.28	6.37	4.33	0.4
Col17-16	42.37	1.18	35.04	12.22	6.83	0.66
Col17-17	73.88	0.33	12.27	5.12	0.08	2.73
Col17-21	74.79	0.74	11.26	6.59	3.27	0.64
Col17-28	51.52	1.05	25.41	11.78	6.42	0.42
Col17-40	61.58	0.74	23.74	6.93	4.48	0.25
Col17-48	68.21	0.54	17.88	5	2.85	1.52
1-24	63.69	0.97	17.72	10.25	3.28	0.13
1-25	65.12	1	17.17	8.8	2.77	0.26

	SiO_2	TiO_2	Al_2O_3	FeO total	MgO	CaO
2-1	65.44	0.97	17.05	8.49	2.64	0.14
2-2	60.37	1.11	20.04	9.23	2.68	0.17
2-3	60.61	1.23	19.34	10.34	2.88	0.15
2-5	62.66	1.06	18.7	10.04	2.79	0.14
2-7	58.32	1.2	20.13	10.9	2.83	0.21
2-17	58.82	0.98	22.89	7.82	4.1	0.44
2-18	61.98	1.11	18.89	9.46	2.74	0.2
2-19	47.66	1.53	28.89	12.15	3.65	1.01
2-20	55.49	1.12	22.06	9.36	2.19	0.36
3-4	66.86	0.59	17.94	6.45	2.05	0.04
3-5	79.32	0.43	11.02	4.26	1.21	0.03
3-6	70.04	0.58	16.73	5.31	1.59	0.02
3-9	70.35	0.59	16.54	5.67	1.5	0.05
3-14	69.93	0.59	17.94	4.78	1.2	0.04
3-17	71.13	0.57	16.47	5.25	1.38	0.03
3-24	74.29	0.52	14.24	4.87	1.22	0.04
ST16-1	82.95	0.26	7.77	1.91	0.56	6.3
ST16-2A	61.22	0.69	21.33	5.93	2.38	0.43
ST16-2B	74.34	0.54	13.54	4.32	1.45	1.06
ST16-3A	76.83	0.3	12.37	2.39	0.82	0.92
ST16-3B	69.78	0.61	15.83	5.36	2.01	0.75
ST16-3C	74.09	0.49	13.77	4.12	1.48	0.84
ST16-4	69.87	0.51	16.92	4.61	1.77	0.62
ST16-5	54.13	0.78	27.79	6.33	2.72	0.6
ST16-9	56.9	0.52	25.36	6.27	2.33	0.36
ST16-13A	57.56	0.82	24.03	7.84	2.83	0.25
ST16-14	57.92	0.77	23.83	6.45	2.53	0.65
ST16-15	50.94	0.57	23.7	16.22	2.81	0.52
ST16-16A	82.49	0.34	9.19	2.17	0.64	3.38
ST16-17	68.39	0.71	16.72	6.3	2.24	0.24
ST16-18	54.51	1	25	9.93	3.34	0.25
ST16-19A	55.46	0.75	25.49	8.7	3.24	0.33

	MnO	K_2O	Na_2O	P_2O_5	Total	LOI
WI-1B	0.19	4.07	1.42	0.08	**100.19**	1.98
WI-7	0.34	3.09	3.12	0.47	**100.34**	1.45
WI-9	0.41	0.87	0.34	0.05	**100.41**	3.02
WI-48	0.13	2.04	2.13	0.06	**100.13**	1.27
WI-62	2.42	0.24	1.47	0.23	**102.42**	0.69
WI-99	0.21	3.55	1.79	0.05	**100.21**	1.19
KM-01	0.17	3.31	2.83	0.07	**100.17**	0.65
KM-07	0.21	4.47	2.57	0.08	**100.21**	0.6
LM-08	0.26	3.62	2.11	0.05	**100.26**	1.39
104a	0.07	3.75	1.42	0.15	**100.07**	1.65
A325/105b	0.18	0.61	3.42	0.04	**100.18**	0.8
A325/81	0.13	0.69	4.62	0.02	**100.13**	0.59
A325/60	0.16	0.58	4.22	0	**100.16**	0.78
A325/148	0.19	0.71	2.99	0.11	**100.19**	0.92
A325/121	0.18	0.55	3.81	0.03	**100.18**	0.8
A325/1105	0.25	0.29	1.88	0.15	**100.25**	0.67
A325/78	0.29	0.19	1.46	0.17	**100.29**	0.78
A325/158	0.2	0.35	1.93	0.13	**100.2**	0.84
A325/1165a	0.06	1.96	4.96	0.04	**100.06**	0.55
A325/1684	0.46	1	3.15	0.41	**100.46**	1.16
A325/1687	0.58	5.7	4.08	0.09	**100.58**	1.7
161-2	0	1.24	2.93	0.15	**100**	1.33
1448	2.99	0.37	2.77	0	**102.99**	1.65
A222-001	0.14	2.68	3.52	0.14	**100.14**	0.85
A222-002	0.07	2.73	2.52	0.19	**100.07**	1
A222-003	0.05	5.6	1.32	0.03	**100.05**	3.07
A222-006	0.04	2.03	2.35	0.15	**100.04**	0.77
A222-007	0.04	3.04	2.28	0.18	**100.04**	0.43
A222-008	0.07	1.73	3.1	0.18	**100.07**	0.71
A222-010	0.02	1.23	2.8	0.04	**100.02**	1.27
A222-011	0.04	2.68	2.4	0.18	**100.04**	0.96
A222-013	0.09	5	1.51	0.18	**100.09**	1.8
A222-014	0.07	1.97	2.55	0.18	**100.07**	0.67
A222-015	0.03	2.57	2.46	0.08	**100.03**	0.57
A222-016	0.08	6.68	0.57	0.13	**100.08**	1.4
A222-017	0.03	2.02	2.21	0.05	**100.03**	0.78
A222-018	0.11	7.15	1.55	0.06	**100.11**	2.74
A222-019	0.03	2.75	2.94	0.07	**100.03**	0.93
A222-020	0.01	1.26	3.91	0.05	**100.01**	0.68
A222-021	0.07	2.61	2.54	0.15	**100.07**	0.63
A222-024	0.07	4.38	2.27	0.07	**100.07**	1.68
CHR124	0	2.24	1.02	0	**100**	
STF 1	0.11	6.09	0.41	0.14	**100.11**	1.74
STF-2a	0.19	6.03	0.39	0.09	**100.19**	1.75
STF-2b	0.13	6.77	0.63	0.13	**100.13**	2.06
STF 4a	0.06	2.44	1.06	0.11	**100.06**	1.11
STF-5	0.09	6.27	0.83	0.14	**100.09**	0.66

	MnO	K_2O	Na_2O	P_2O_5	Total	LOI
STF-6	0.12	6.62	1	0.13	**100.12**	1.45
STF-8	0.11	3.16	0.73	0.1	**100.11**	0.85
STF-9	0.09	6.58	1.47	0.16	**100.09**	0.89
STF-11	0.08	4.43	1.04	0.11	**100.08**	1.01
STF-12	0.07	7.37	1.61	0.13	**100.07**	1.57
STF-13	0.06	4.45	1.56	0.1	**100.06**	1.07
STF-16a	0.06	6.75	1.25	0.13	**100.06**	0.72
STF-16b	0.09	5.66	0.91	0.13	**100.09**	1.3
STF-17a	0.06	4.4	0.47	0.09	**100.06**	1.08
STF-17b	0.07	4.44	0.52	0.12	**100.07**	1.07
STF-18a	0.07	8.13	1.61	0.14	**100.07**	0.47
STF-18b	0.07	7.55	1.29	0.12	**100.07**	0.59
STF-18c	0.08	6.64	1.14	0.13	**100.08**	1.21
STF-18d	0.07	3.31	0.67	0.13	**100.07**	0.49
STF-20	0.06	2.71	1.42	0.11	**100.06**	0.73
STF-21a	0.06	3.02	1.1	0.11	**100.06**	0.5
STF-21b	0.05	3.24	0.76	0.11	**100.05**	0.52
STF-21c	0.09	6.33	1.24	0.12	**100.09**	0.6
STF-26a	0.11	2.4	0.6	0.1	**100.11**	1.25
STF-26b	0.09	1.95	0.95	0.1	**100.09**	0.09
STF-27	0.08	3.28	1.42	0.11	**100.08**	1.63
STF-28	0.05	7.04	1.07	0.12	**100.05**	1.38
STF-29	0.08	2.05	1.48	0.09	**100.08**	0.65
STF 30	0.64	4.8	2.91	0.13	**100.64**	2.23
STF 31a	0.06	3.41	1.5	0.1	**100.06**	1.34
STF-32	0.03	5.38	0.79	0.11	**100.03**	0.82
ST16-31A	0.05	2.77	1.24	0.1	**100.05**	0.7
IV16-02	0.15	4.3	3.41	0.17	**100.15**	
IV16-03A	0.14	4.35	0.47	0.05	**100.14**	
IV16-04	0.13	2.67	0.85	0.33	**100.13**	
IV16-05	0.09	3	2.82	0.18	**100.09**	
IV16-06	0.09	2.22	4.54	0.13	**100.09**	
IV16-08	0.19	3.99	1.23	0.17	**100.19**	
IV16-09A	0.11	1.44	0.49	0.19	**100.11**	
IV16-10	0.18	3.07	0.99	0.11	**100.18**	
IV16-11	0.28	1.59	1.74	0.2	**100.28**	
IV16-12	0.26	3.24	0.74	0.15	**100.26**	
IV16-13A	0.13	3.73	1.91	0.12	**100.13**	
IV16-14	0.26	2.92	3.72	0.09	**100.26**	
IV16-15	0.16	0.92	1.72	0.46	**100.16**	
IV16-16	0.13	1.41	0.58	0.05	**100.13**	
IV16-17A	0.31	2.26	0.61	0.08	**100.31**	
IV16-18	0.13	2.14	0.25	0.04	**100.13**	
IV16-21	0.07	2.87	3.16	0.16	**100.07**	
IV16-24	0.17	1.72	1.12	0.05	**100.17**	
IV16-26	0.08	3.74	1.02	0.07	**100.08**	
SQ17-02	0.05	2.7	2.32	0.19	**100.05**	2.41

	MnO	K_2O	Na_2O	P_2O_5	Total	LOI
SQ17-04	0.06	4.94	1.07	0.2	**100.06**	3.86
SQ17-07	0.18	2.46	2.3	0.18	**100.18**	7.92
SQ17-08	0.21	3.5	1.42	0.18	**100.21**	8.71
SQ17-09	0.09	2.48	3.26	0.08	**100.09**	0.5
SQ17-10	0.08	3.58	2.02	0.2	**100.08**	1.34
SQ17-11	0.12	3.78	2.49	0.15	**100.12**	0.89
SQ17-12	0.09	2.07	2.49	0.24	**100.09**	0.48
SQ17-14	0.04	4.41	2.43	0.07	**100.04**	0.51
SQ17-15	0.17	0.18	0.42	0.28	**100.17**	1.14
SQ17-17	0.09	0.66	1.6	0.12	**100.09**	0.51
SQ17-19	0.1	2.54	2.75	0.5	**100.1**	0.54
SQ17-20	0.07	2.37	2.5	0.24	**100.07**	0.33
SQ17-21	0.09	3.23	2.65	0.18	**100.09**	0.49
SQ17-22	0.1	2.89	2.4	0.18	**100.1**	0.59
SQ17-24	0.08	2.15	3.28	0.16	**100.08**	0.49
SQ17-25	0.13	5.02	2.46	0.21	**100.13**	1.59
SQ17-26	0.08	2.35	2.35	0.27	**100.08**	0.44
SQ17-27	0.12	3.47	2.18	0.1	**100.12**	0.73
SQ17-28	0.08	2.14	2.05	0.24	**100.08**	0.45
SQ17-29	0.14	4.47	2.02	0.2	**100.14**	0.87
SQ17-30	0.11	3.62	2.82	0.25	**100.11**	0.77
SQ17-31	0.14	4.2	1.46	0.12	**100.14**	1.09
SQ17-32	0.1	3.13	1.94	0.19	**100.1**	0.79
SQ17-33	0.06	3.24	2.22	0.06	**100.06**	0.49
SQ17-34	0.12	6.1	2.66	0.13	**100.12**	0.16
SQ17-37	0.06	3.94	2.18	0.09	**100.06**	0.34
SQ17-38	0.12	3.8	2.02	0.17	**100.12**	1.16
SQ17-39	0.12	2.93	2.4	0.17	**100.12**	0.69
SQ17-40	0.08	4.19	1.79	0.13	**100.08**	0.96
SQ17-41	0.06	5.11	3.03	0.12	**100.06**	0.75
SQ17-42	0.09	3.54	2.08	0.11	**100.09**	0.65
SQ17-43	0.17	3.25	2.08	0.08	**100.17**	0.6
Col17-3	0.05	3.11	0.44	0.03	**100.05**	1.8
Col17-4	0.1	2.18	0.51	0.03	**100.1**	1.16
Col17-16	0.1	1.38	0.3	0.03	**100.1**	1.35
Col17-17	0.06	1.8	3.74	0.05	**100.06**	0.34
Col17-21	0.16	1.69	0.8	0.23	**100.16**	1.8
Col17-28	0.23	3.01	0.35	0.04	**100.23**	2.7
Col17-40	0.12	1.92	0.33	0.03	**100.12**	0.93
Col17-48	0.09	1.75	2.22	0.03	**100.09**	1.18
1-24	0.05	3.24	0.65	0.07	**100.05**	1.3
1-25	0.05	3.95	0.86	0.06	**100.05**	0.88
2-1	0.05	4.34	0.86	0.07	**100.05**	1.05
2-2	0.04	5.35	0.99	0.07	**100.04**	1.18
2-3	0.04	4.54	0.85	0.07	**100.04**	0.92
2-5	0.04	3.85	0.67	0.08	**100.04**	0.87
2-7	0.03	5.23	1.12	0.07	**100.03**	0.96

	MnO	K_2O	Na_2O	P_2O_5	Total	LOI
2-17	0.04	4.48	0.33	0.13	**100.04**	0.96
2-18	0.07	4.65	0.88	0.08	**100.07**	0.73
2-19	0.04	2.95	2.04	0.12	**100.04**	0.71
2-20	0.04	7.99	1.29	0.14	**100.04**	0.75
3-4	0.05	5.81	0.23	0.04	**100.05**	2.38
3-5	0.04	3.57	0.11	0.04	**100.04**	1.66
3-6	0.04	5.52	0.15	0.04	**100.04**	2.21
3-9	0.03	5.11	0.15	0.04	**100.03**	2.3
3-14	0.02	5.31	0.16	0.04	**100.02**	2.67
3-17	0.04	4.96	0.15	0.05	**100.04**	2.36
3-24	0.03	4.61	0.13	0.08	**100.03**	2.15
ST16-1	0.33	0.02	0.15	0.08	**100.33**	0.35
ST16-2A	0.09	6.44	1.46	0.13	**100.09**	1.33
ST16-2B	0.07	3.27	1.33	0.14	**100.07**	1.18
ST16-3A	0.05	4.31	1.93	0.14	**100.05**	0.61
ST16-3B	0.1	4.37	1.2	0.08	**100.1**	1.1
ST16-3C	0.07	3.64	1.49	0.07	**100.07**	0.95
ST16-4	0.06	4.08	1.54	0.09	**100.06**	1.15
ST16-5	0.09	5.91	1.59	0.16	**100.09**	1.12
ST16-9	0.1	6.72	1.38	0.15	**100.1**	1.16
ST16-13A	0.08	5.25	1.29	0.12	**100.08**	1.52
ST16-14	0.08	5.89	1.84	0.12	**100.08**	3.15
ST16-15	0.2	3.93	1.2	0.11	**100.2**	2.36
ST16-16A	0.13	0.23	1.42	0.14	**100.13**	0.28
ST16-17	0.07	4.44	0.86	0.1	**100.07**	0.46
ST16-18	0.25	4.64	1.22	0.1	**100.25**	1.43
ST16-19A	0.11	4.64	1.18	0.2	**100.11**	0.75

APPENDIX F: MINERAL ASSEMBLAGES

	K-Feldspar	Plagioclase	Garnet	Biotite	Quartz	Cordierite
WI-1B			✓	✓	✓	✓
WI-7	✓	✓	✓	✓	✓	✓
WI-9						✓
WI-48			✓	✓		✓
WI-62			✓			
WI-99			✓			✓
KM-01			✓	✓		✓
KM-07			✓			
LM-08	✓		✓	✓	✓	
104a			✓	✓	✓	
A325/105b		✓		✓	✓	
A325/81		✓			✓	
A325/60		✓		✓	✓	
A325/148		✓		✓	✓	
A325/121		✓		✓	✓	
A325/1105		✓	✓			
A325/78		✓				
A325/158		✓		✓	✓	
A325/1165a	✓	✓			✓	
A325/1684		✓		✓	✓	
A325/1687		✓	✓	✓		
161-2						
1448						
A222-001						
A222-002						
A222-003						
A222-006						
A222-007						
A222-008						
A222-010						
A222-011						
A222-013						
A222-014						
A222-015						
A222-016						
A222-017						
A222-018						
A222-019						
A222-020						
A222-021						

	K-Feldspar	Plagioclase	Garnet	Biotite	Quartz	Cordierite
A222-024						
CHR124						
STF 1				✓		
STF-2a				✓		
STF-2b	✓			✓	✓	
STF 4a						
STF-5						✓
STF-6						✓
STF-8				✓		✓
STF-9	✓			✓		✓
STF-11						✓
STF-12						✓
STF-13				✓		✓
STF-16a	✓			✓	✓	✓
STF-16b			✓	✓		✓
STF-17a						✓
STF-17b						✓
STF-18a	✓					
STF-18b				✓		✓
STF-18c				✓		✓
STF-18d				✓		✓
STF-20					✓	
STF-21a					✓	
STF-21b				✓		
STF-21c						
STF-26a						
STF-26b						
STF-27					✓	
STF-28	✓					✓
STF-29			✓		✓	
STF 30			✓			
STF 31a						
STF-32					✓	
ST16-31A	✓			✓	✓	
IV16-02						
IV16-03A		✓	✓	✓	✓	
IV16-04						
IV16-05						
IV16-06						
IV16-08		✓	✓	✓	✓	
IV16-09A						
IV16-10						
IV16-11						
IV16-12		✓	✓	✓	✓	

	K-Feldspar	Plagioclase	Garnet	Biotite	Quartz	Cordierite
IV16-13A						
IV16-14						
IV16-15						
IV16-16	✓	✓	✓	✓	✓	
IV16-17A						
IV16-18						
IV16-21						
IV16-24						
IV16-26						
SQ17-02						
SQ17-04						
SQ17-07						
SQ17-08						
SQ17-09						
SQ17-10				✓		✓
SQ17-11						
SQ17-12				✓		
SQ17-14			✓	✓		
SQ17-15						
SQ17-17						
SQ17-19			✓			✓
SQ17-20						
SQ17-21						
SQ17-22				✓		
SQ17-24						
SQ17-25				✓		✓
SQ17-26						
SQ17-27				✓		
SQ17-28				✓		
SQ17-29				✓		
SQ17-30						
SQ17-31				✓		✓
SQ17-32	✓					✓
SQ17-33	✓		✓	✓		✓
SQ17-34			✓			✓
SQ17-37	✓		✓	✓		✓
SQ17-38						✓
SQ17-39						✓
SQ17-40				✓		✓
SQ17-41				✓		✓
SQ17-42			✓			✓
SQ17-43			✓			✓
Col17-3		✓	✓	✓	✓	
Col17-4		✓	✓	✓	✓	

	K-Feldspar	Plagioclase	Garnet	Biotite	Quartz	Cordierite
Col17-16		✓	✓	✓	✓	
Col17-17		✓	✓	✓	✓	
Col17-21		✓	✓	✓	✓	
Col17-28		✓	✓	✓		
Col17-40		✓	✓	✓	✓	
Col17-48		✓	✓	✓	✓	
1-24				✓	✓	
1-25				✓	✓	
2-1	✓			✓	✓	✓
2-2	✓			✓	✓	✓
2-3	✓			✓	✓	✓
2-5	✓			✓	✓	✓
2-7	✓			✓	✓	✓
2-17	✓			✓	✓	✓
2-18	✓			✓	✓	✓
2-19	✓			✓	✓	✓
2-20	✓			✓	✓	✓
3-4				✓	✓	
3-5				✓	✓	
3-6				✓	✓	
3-9				✓	✓	
3-14				✓	✓	
3-17				✓	✓	
3-24				✓	✓	
ST16-1						
ST16-2A						
ST16-2B						
ST16-3A						
ST16-3B						
ST16-3C	✓	✓		✓	✓	✓
ST16-4						
ST16-5						
ST16-9	✓	✓		✓	✓	✓
ST16-13A						
ST16-14						
ST16-15						
ST16-16A						
ST16-17						
ST16-18						
ST16-19A	✓	✓	✓	✓	✓	✓

	Opx	Cpx	Sillimanite	Andalusite	Kyanite	Staurolite
WI-1B						
WI-7						
WI-9						
WI-48			✓			
WI-62	✓					
WI-99	✓					
KM-01						
KM-07						
LM-08						
104a				✓		✓
A325/105b	✓	✓				
A325/81	✓	✓				
A325/60	✓	✓				
A325/148	✓	✓				
A325/121	✓	✓				
A325/1105	✓	✓				
A325/78	✓	✓				
A325/158	✓	✓				
A325/1165a	✓					
A325/1684						
A325/1687						
161-2						
1448						
A222-001						
A222-002						
A222-003						
A222-006						
A222-007						
A222-008						
A222-010						
A222-011						
A222-013						
A222-014						
A222-015						
A222-016						
A222-017						
A222-018						
A222-019						
A222-020						
A222-021						
A222-024						
CHR124						
STF 1						
STF-2a				✓		

	Opx	Cpx	Sillimanite	Andalusite	Kyanite	Staurolite
STF-2b				✓		
STF 4a						
STF-5						
STF-6						
STF-8						
STF-9				✓		
STF-11				✓		
STF-12			✓	✓		
STF-13						
STF-16a			✓	✓		
STF-16b						
STF-17a						
STF-17b						
STF-18a						
STF-18b						
STF-18c						
STF-18d						
STF-20						
STF-21a						
STF-21b						
STF-21c						
STF-26a						
STF-26b						
STF-27	✓					
STF-28						
STF-29						
STF 30						
STF 31a						
STF-32						
ST16-31A						
IV16-02						
IV16-03A						
IV16-04						
IV16-05						
IV16-06						
IV16-08			✓			
IV16-09A						
IV16-10						
IV16-11						
IV16-12			✓			
IV16-13A						
IV16-14						
IV16-15						
IV16-16			✓			

	Opx	Cpx	Sillimanite	Andalusite	Kyanite	Staurolite
IV16-17A						
IV16-18						
IV16-21						
IV16-24						
IV16-26						
SQ17-02						
SQ17-04						
SQ17-07						
SQ17-08						
SQ17-09						
SQ17-10						
SQ17-11						
SQ17-12						
SQ17-14			✓			
SQ17-15						
SQ17-17						
SQ17-19	✓					
SQ17-20						
SQ17-21						
SQ17-22			✓			
SQ17-24						
SQ17-25						
SQ17-26						
SQ17-27						
SQ17-28						
SQ17-29						
SQ17-30						
SQ17-31			✓			
SQ17-32						
SQ17-33	✓					
SQ17-34	✓					
SQ17-37	✓					
SQ17-38			✓			
SQ17-39						
SQ17-40			✓			
SQ17-41			✓			
SQ17-42						
SQ17-43						
Col17-3					✓	
Col17-4			✓		✓	
Col17-16					✓	
Col17-17						
Col17-21					✓	✓
Col17-28					✓	

	Opx	Cpx	Sillimanite	Andalusite	Kyanite	Staurolite
Col17-40					✓	
Col17-48					✓	
1-24				✓		
1-25				✓		
2-1			✓			
2-2			✓			
2-3			✓			
2-5			✓			
2-7			✓			
2-17			✓			
2-18			✓			
2-19			✓			
2-20			✓			
3-4				✓		
3-5				✓		
3-6				✓		
3-9				✓		
3-14				✓		
3-17				✓		
3-24				✓		
ST16-1						
ST16-2A						
ST16-2B						
ST16-3A						
ST16-3B						
ST16-3C			✓			
ST16-4						
ST16-5						
ST16-9			✓			
ST16-13A						
ST16-14						
ST16-15						
ST16-16A						
ST16-17						
ST16-18						
ST16-19A			✓			

	Hornblende	Magnetite	Ilmentie	Tourmaline	Scapolite
WI-1B					
WI-7					
WI-9					
WI-48					
WI-62					
WI-99					
KM-01					
KM-07					
LM-08					
104a					
A325/105b					
A325/81					
A325/60					
A325/148					
A325/121					
A325/1105	✓				
A325/78					✓
A325/158					
A325/1165a					
A325/1684	✓				
A325/1687					
161-2					
1448					
A222-001					
A222-002					
A222-003					
A222-006					
A222-007					
A222-008					
A222-010					
A222-011					
A222-013					
A222-014					
A222-015					
A222-016					
A222-017					
A222-018					
A222-019					
A222-020					
A222-021					
A222-024					
CHR124					
STF 1					
STF-2a					

	Hornblende	Magnetite	Ilmentie	Tourmaline	Scapolite
STF-2b			✓		
STF 4a					
STF-5					
STF-6					
STF-8					
STF-9					
STF-11					
STF-12					
STF-13					
STF-16a			✓		
STF-16b					
STF-17a					
STF-17b					
STF-18a					
STF-18b					
STF-18c					
STF-18d					
STF-20					
STF-21a					
STF-21b					
STF-21c					
STF-26a					
STF-26b					
STF-27					
STF-28					
STF-29					
STF 30					
STF 31a					
STF-32					
ST16-31A				✓	
IV16-02					
IV16-03A					
IV16-04					
IV16-05					
IV16-06					
IV16-08					
IV16-09A					
IV16-10					
IV16-11					
IV16-12					
IV16-13A					
IV16-14					
IV16-15					
IV16-16					

	Hornblende	Magnetite	Ilmentie	Tourmaline	Scapolite
IV16-17A					
IV16-18					
IV16-21					
IV16-24					
IV16-26					
SQ17-02					
SQ17-04					
SQ17-07					
SQ17-08					
SQ17-09					
SQ17-10					
SQ17-11					
SQ17-12					
SQ17-14					
SQ17-15					
SQ17-17					
SQ17-19					
SQ17-20					
SQ17-21					
SQ17-22					
SQ17-24					
SQ17-25					
SQ17-26					
SQ17-27					
SQ17-28					
SQ17-29					
SQ17-30					
SQ17-31					
SQ17-32					
SQ17-33					
SQ17-34					
SQ17-37					
SQ17-38					
SQ17-39					
SQ17-40					
SQ17-41					
SQ17-42					
SQ17-43					
Col17-3					
Col17-4					
Col17-16					
Col17-17					
Col17-21					
Col17-28					

	Hornblende	Magnetite	Ilmentie	Tourmaline	Scapolite
Col17-40					
Col17-48					
1-24		✓	✓		
1-25		✓	✓		
2-1		✓	✓		
2-2		✓	✓		
2-3		✓	✓		
2-5		✓	✓		
2-7		✓	✓		
2-17		✓	✓		
2-18		✓	✓		
2-19		✓	✓		
2-20		✓	✓		
3-4			✓		
3-5			✓		
3-6			✓		
3-9			✓		
3-14			✓		
3-17			✓		
3-24			✓		
ST16-1					
ST16-2A					
ST16-2B					
ST16-3A					
ST16-3B					
ST16-3C			✓	✓	
ST16-4					
ST16-5					
ST16-9			✓	✓	
ST16-13A					
ST16-14					
ST16-15					
ST16-16A					
ST16-17					
ST16-18					
ST16-19A			✓		

	Corundum	Rutile	Graphite	Muscovite	Chlorite
WI-1B					
WI-7					
WI-9					
WI-48					
WI-62					
WI-99					
KM-01					
KM-07					
LM-08					
104a				✓	
A325/105b					
A325/81					
A325/60					
A325/148					
A325/121					
A325/1105					
A325/78					
A325/158					
A325/1165a					
A325/1684					
A325/1687	✓			✓	
161-2					
1448					
A222-001					
A222-002					
A222-003					
A222-006					
A222-007					
A222-008					
A222-010					
A222-011					
A222-013					
A222-014					
A222-015					
A222-016					
A222-017					
A222-018					
A222-019					
A222-020					
A222-021					
A222-024					
CHR124					
STF 1					
STF-2a					

	Corundum	Rutile	Graphite	Muscovite	Chlorite
STF-2b				✓	
STF 4a				✓	
STF-5					
STF-6					
STF-8					
STF-9					
STF-11					
STF-12					
STF-13					
STF-16a					
STF-16b					
STF-17a					
STF-17b					
STF-18a					
STF-18b					
STF-18c					
STF-18d					
STF-20					
STF-21a					
STF-21b					
STF-21c					
STF-26a					
STF-26b					
STF-27					
STF-28					
STF-29					
STF 30					
STF 31a				✓	
STF-32					
ST16-31A				✓	
IV16-02					
IV16-03A				✓	
IV16-04					
IV16-05					
IV16-06					
IV16-08				✓	
IV16-09A					
IV16-10					
IV16-11					
IV16-12		✓		✓	
IV16-13A					
IV16-14					
IV16-15					
IV16-16		✓	✓		

	Corundum	Rutile	Graphite	Muscovite	Chlorite
IV16-17A					
IV16-18					
IV16-21					
IV16-24					
IV16-26					
SQ17-02					
SQ17-04					✓
SQ17-07					
SQ17-08					✓
SQ17-09					
SQ17-10				✓	
SQ17-11					
SQ17-12				✓	
SQ17-14					
SQ17-15					
SQ17-17					
SQ17-19					
SQ17-20					
SQ17-21					
SQ17-22					
SQ17-24					
SQ17-25					
SQ17-26					
SQ17-27				✓	
SQ17-28					
SQ17-29					
SQ17-30					
SQ17-31					
SQ17-32					
SQ17-33					
SQ17-34					
SQ17-37					
SQ17-38					
SQ17-39					
SQ17-40					
SQ17-41					
SQ17-42					
SQ17-43					
Col17-3					
Col17-4					
Col17-16					
Col17-17					
Col17-21					
Col17-28					

	Corundum	Rutile	Graphite	Muscovite	Chlorite
Col17-40					
Col17-48					
1-24					
1-25					
2-1					
2-2					
2-3					
2-5					
2-7					
2-17					
2-18					
2-19					
2-20					
3-4				✓	
3-5				✓	
3-6				✓	
3-9				✓	
3-14				✓	
3-17				✓	
3-24				✓	
ST16-1					
ST16-2A					
ST16-2B					
ST16-3A					
ST16-3B					
ST16-3C				✓	
ST16-4					
ST16-5					
ST16-9					
ST16-13A					
ST16-14					
ST16-15					
ST16-16A					
ST16-17					
ST16-18					
ST16-19A					